ANNUAL REVIEWS

Annual Review of Materials Research

Design and Characterization of Host Frameworks for Facile Magnesium Transport

Yirong Gao,[1] Tara P. Mishra,[2,3] Shou-Hang Bo,[1,4] Gopalakrishnan Sai Gautam,[5] and Pieremanuele Canepa[2,3,6]

[1] University of Michigan–Shanghai Jiao Tong University Joint Institute, Shanghai Jiao Tong University, Shanghai, China; email: shouhang.bo@sjtu.edu.cn

[2] Department of Materials Science and Engineering, National University of Singapore, Singapore; email: pcanepa@nus.edu.sg

[3] Singapore-MIT Alliance for Research and Technology, Singapore

[4] School of Chemistry and Chemical Engineering, Shanghai Jiao Tong University, Shanghai, China

[5] Department of Materials Engineering, Indian Institute of Science, Bangalore, India; email: saigautamg@iisc.ac.in

[6] Department of Chemical and Biomolecular Engineering, National University of Singapore, Singapore

ANNUAL REVIEWS **CONNECT**

www.annualreviews.org

- Download figures
- Navigate cited references
- Keyword search
- Explore related articles
- Share via email or social media

Keywords

ion transport, host frameworks, characterization, magnesium batteries

Abstract

The development of inexpensive batteries based on magnesium (Mg) chemistry will contribute remarkably toward developing high-energy-density storage systems that can be used worldwide. Significant challenges remain in developing practical Mg batteries, the chief of which is designing materials that can provide facile transport of Mg. In this review, we cover the experimental and theoretical methods that can be used to quantify Mg mobility in a variety of host frameworks, the specific transport quantities that each technique is designed to measure or calculate, and some practical examples of their applications. We then list the unique challenges faced by different experimental and computational techniques in probing Mg ion transport in materials. This review concludes with an outlook on the directions that the scientific community could soon pursue as we strive to construct a pragmatic Mg battery.

1. SETTING THE SCENE

Energy storage is an important complementary technology that is essential for a successful transition into a fossil fuel–free and sustainable future (1–4). Developing energy storage technology that will make portable electronics, vehicular transportation, and electric grids more efficient and less reliant on fossil fuels is paramount. The current state of the art in energy storage is lithium (Li)-ion batteries, which are approaching their practically achievable limits of energy density (4). Li-ion batteries have other important technological drawbacks as well, including safety [usage of flammable electrolytes and electrodes susceptible to oxygen release (5)], their usage of supply-constrained metals [Li and more importantly cobalt (Co) and nickel (Ni)], and the expense of current collectors [copper (Cu)] (6). Hence, it is important to develop battery systems that explore chemistries beyond Li-ion systems while achieving better safety and comparable energy densities with minimal supply constraints.

One promising avenue beyond Li-ion battery systems is based on multivalent (MV) chemistry, such as magnesium (Mg), calcium (Ca), zinc (Zn), and aluminum (Al). In MV systems, the ion transported across electrodes (Mg^{2+}, Ca^{2+}, Zn^{2+}, or Al^{3+}) has a higher oxidation state compared with Li^+. From a theoretical standpoint, this results in a multielectron transfer across the external circuit for each cation transferred (7–9).

Although in theory the (de)intercalation of each MV species in an electrode corresponds to the exchange of at least twice the amount of electrons compared with monovalent Li systems, the real gain in energy density in MV systems arises from the usage of the metal anode (7, 8). Specifically, compared with Li metal or Li in graphite, using Mg or Al metal as the anode results in a significantly higher volumetric capacity [3,833 mAh/cm^3 for Mg, 8,040 mAh/cm^3 for Al, 2,046 mAh/cm^3 for Li metal, and 800 mAh/cm^3 for Li in graphite (8)], which can result in superior volumetric energy densities than current Li-ion batteries. Note that most MV metals, such as Mg, appear more resistant to dendritic nucleation and growth during typical battery charging conditions compared with Li metal and may be slightly safer to operate (10).

Therefore, if the transition metal species used in the positive electrode (cathode) is not supply constrained (e.g., Co), MV batteries should be less susceptible to any (future) geopolitical restrictions and consequently less expensive in the long run. Given the bigger focus on Mg-based chemistries among MV systems in the literature (8), this review focuses on Mg-based compounds and structures. However, many of the trends observed in Mg should be applicable to other MV systems as well.

Another pathway to improving the safety aspects of batteries in general is to replace the flammable, organic liquid electrolytes that are typically used with nonflammable, safer solid electrolytes (e.g., fast solid ionic conductors). Using solid electrolytes also has the potential to improve the energy densities of batteries since they may enable the usage of a metal electrode by reducing the susceptibility of dendrite formation, resulting in superior volumetric capacities and energy densities.

However, the design of Mg-based solid electrolytes is constrained by multiple factors. For example, a practical solid electrolyte should not only exhibit an ionic conductivity that is comparable to that of liquid electrolytes ($\sim 10^{-2}$ to 10^{-4} S/cm) (11, 12) but also be electrochemically stable across a wide voltage range (13), exhibit low electronic conductivity, and prevent the nucleation and propagation of dendrites (14). Despite these challenges, significant progress has been made in the development of solid electrolytes for Li-ion systems (14–16). The usage of a solid electrolyte in conjunction with a Mg metal negative electrode (anode) and a high-voltage cathode will mark a significant leap in achievable energy densities and safety standards. Hence, developing solid-state Mg ionic conductors is also an important step in the development of Mg batteries.

Despite the promises of Mg batteries, significant challenges remain in their construction. For example, reliable liquid electrolytes that are stable against the metal anode and a high-voltage cathode (~3.5 V or higher) is still an active area of development (7, 17–19). Another important challenge is the development of solid host materials with good Mg ionic conductivity, which can be utilized either as cathode electrodes or solid electrolytes. Good ion transport within solid electrodes or electrolytes is a vital prerequisite for a battery framework to operate at high (dis)charge rates. In general, Mg ions diffuse slower through ionic lattices, especially when the anion is O^{2-} (20–22), and this has been attributed to higher local electrostatic distortions in the past (7). A facile Mg ionic conductor can be used as an electrode if it contains a redox-active species (typically a 3d/4d metal), while it can be used as a solid electrolyte or a coating material if it does not contain a redox-active species and exhibits low electronic conductivity. Thus, developing facile solid Mg conductors will, in general, accelerate the development and deployment of Mg batteries.

In spite of widespread attempts to develop materials with facile Mg ion conductivity, only a handful of cathode materials have been shown to reversibly intercalate Mg ions at reasonable (dis)charge rates, including chevrel-Mo_6S_8 (23), layered-V_2O_5 (24–27), and spinel-Ti_2S_4 (28–32). Other cathode candidates that have been proposed suffer from poor thermodynamic stability (e.g., Mg in postspinel frameworks and $Mg_xCr_2O_4$) (33, 34), side reactions (e.g., Mg in hollandite-MnO_2) (35, 36), defects (e.g., spinel inversion in $Mg_xMn_2O_4$) (37–39), electrolyte stability challenges (e.g., Ca systems; also observed in Mg chemistries) (40), and solvent cointercalation (e.g., Mg and Zn in V_2O_5) (41, 42). A few theoretical studies have proposed new ionic conductors for Mg (and Ca) systems (43–45), but these systems have not yet been experimentally tested.

In the case of solid electrolytes, spinel frameworks with Mg^{2+} mobility that are similar to Li^+ have been discovered (46), but the lack of electrochemical stability and significant presence of defects (47–49) plague their practical deployment. Finally, fundamental design principles that can be used to systematically design fast Mg (and MV in general) conductors are still lacking. For example, previous studies have shown that structures hosting cations in a frustrated coordination environment (20, 46) and structures that exhibit large volumes per cation can be fast Mg/MV diffusers, but notable exceptions to such rules do exist (45).

Here, we cover the research that has been done toward designing and understanding transport of Mg ions in host materials. While the focus is predominantly on Mg-based systems, similar trends have been observed in other MV systems as well. Initially, we provide an overview of the underlying physics of ion transport in host frameworks and the various observables that are used to quantify ion mobility, such as migration barriers, diffusivities, and ionic conductivities (Section 2). Subsequently, we delve deep into the experimental (Section 3) and theoretical (Section 4) techniques that are commonly used to probe Mg ion transport, the specific transport quantities that can be measured or calculated using such techniques, and some practical examples of their use in materials so far. In Section 5, we discuss some of the general challenges encountered, both theoretically and experimentally, in assessing Mg transport in materials and offer some suggestions to overcome existing bottlenecks. We provide a set of future directions in Section 6, which the scientific community might find useful for designing better Mg conductors. We are optimistic that our review provides a robust overview of theory, techniques, and applications and will thus form an important step in the practical deployment of materials for Mg batteries.

2. FUNDAMENTALS OF ION TRANSPORT

Ion transport in a crystalline solid—an ordered arrangement of atoms—is caused by a series of microscopic migration events, which can occur via one of the mechanisms shown in **Figure 1a**. These migration mechanisms are based on (a) vacancy diffusion where a lattice ion migrates into a
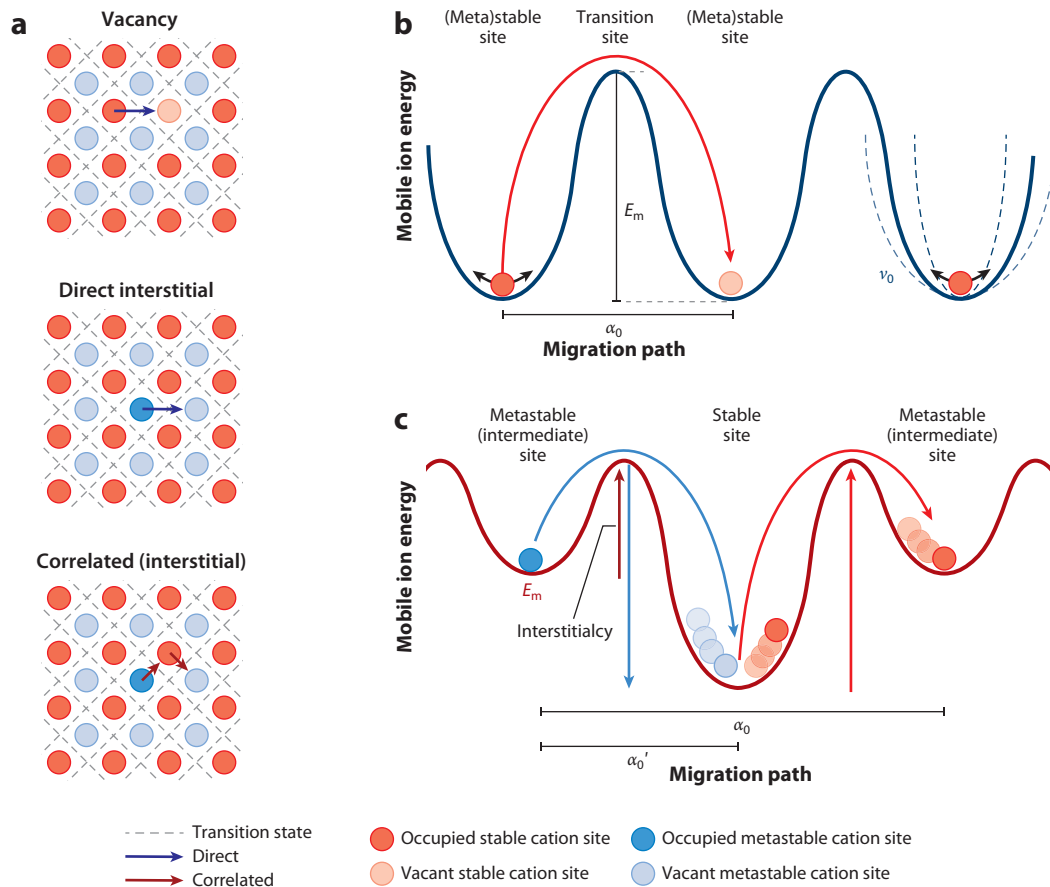
Figure 1

(*a*) Types of ion migration mechanisms that are active in a host material. (*b*) Energy landscape in host materials where ion migration occurs via a metastable transition state. Dashed lines indicate the hardness or softness of the potential well related to the hop frequency v_0. The vector of the migration pathway from one (meta)stable site to another is denoted as α_0. (*c*) Energy landscape in a host material where migration occurs via both a metastable transition and an intermediate site. α_0 and α_0' denote the migration pathway between two metastable sites and between a metastable site and stable site, respectively. The energy barrier associated to the event of ion migration is denoted as E_m. Figure adapted from Reference 15; copyright 2019 Springer Nature.

neighboring vacant site, (*b*) direct interstitial diffusion where a cation hops from an interstitial site to a neighboring interstitial vacancy site, and (*c*) correlated interstitial (or knock-on) migration where the migration of the interstitial ion displaces a neighboring lattice ion into an adjacent interstitial site. The energy landscape of the specific migration mechanism active in each host material determines the ease of migration of ions within the solid.

Ionic conductivity (σ) is the primary descriptor of ion transport of a MV (or monovalent) ion in an anion host lattice. In a rigid anion framework, σ depends solely on the charge (z), concentration (C), and mobility (u) of the MV ion in the solid lattice, as shown in Equation 1. Ion transport is typically a thermally activated process and follows a (modified) Arrhenius relation:

$$\sigma = zCu = \sigma_0 T^m e^{\left(-\frac{E_m + E_f}{k_B T}\right)}. \qquad 1.$$

a First Fick's law

$$J = -D_C \nabla C$$
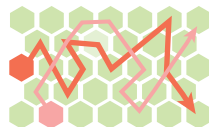
Observables

b Chemical diffusivity

$$D_C = \Theta \, D_J$$

d Jump diffusivity

$$D_J = \frac{1}{2dNt} \left\langle \left(\sum_i r_i(t) \right)^2 \right\rangle$$

f Tracer diffusivity

$$D^* = \frac{\sum_i \langle r_i^2 \rangle}{2dNt}$$

c Thermodynamic factor

$$\Theta = \frac{\partial \left(\frac{\mu}{k_B T} \right)}{\partial \ln x}$$

e Ionic conductivity

$$\sigma = ze^2 C \, \frac{D_J}{k_B T}$$

g Dimensionality of chemical diffusivity

$$D_C \propto \frac{l^2}{t}$$

Figure 2

Governing equations and physical observables describing ionic diffusion, conduction, and their relationships. The quantities indicated are the diffusion flux (J), chemical diffusivity (D_C), the thermodynamic factor (Θ), the jump diffusivity (D_J), the ionic conductivity (σ), the tracer diffusivity (D^*), and dimensionality of chemical diffusivity. Terms appearing in the equations are: μ, the chemical potential of the migrating species; C, the concentration of the mobile ions; z, the charge of the diffusing species; d, the dimensionality of the migration process; k_B, the Boltzmann constant; N, the number of diffusing species; r_i, the displacement of the ith diffusing atom; T, the temperature; t, the time taken for diffusion; x, the site fraction of migrating species; and l, the diffusion length. The diagram at the top right shows a schematic of two random walkers in a rigid lattice.

The power (m) of temperature (T) in Equation 1 typically assumes the value of -1, k_B is the Boltzmann constant, E_m is the energy barrier for migration, E_f is the energy required for the formation of mobile defects, and σ_0 is the pre-exponential constant that is often assumed to be temperature and E_m or E_f independent. The migration barrier corresponds to the highest energy experienced by the migrating ion along the migration pathway connecting two stable sites, that is, the difference in energy between a given stable site and the transition state as the ion migrates through the anion host, as illustrated in **Figure 1b,c**.

Regardless of the active diffusion mechanism, under steady-state conditions, the diffusive flux, J, of MV or monovalent ions along a concentration gradient (∇C) is given by Fick's first law (**Figure 2a**) (50, 51). The chemical diffusion coefficient (D_C) in this equation is the product of the thermodynamic factor (Θ) and the jump diffusion coefficient (D_J) of the chemical diffusivity equation in **Figure 2b**. The ideality versus nonideality of the interactions between the diffusing species (i.e., Mg^{2+}) and the diffusion carriers (vacancies or interstitials) is governed by Θ and is given by the equation in **Figure 2c**, where μ and x are the chemical potential and site fraction of the migrating ion, respectively.

While calculating Θ, it is important to note that x is calculated as the fraction of the ionic sites that are occupied by the mobile species per formula unit of the host. For example, in spinel-$Mg_xMn_2O_4$, each formula unit of Mn_2O_4 has 1 mole of intercalant tetrahedral sites and can accommodate a maximum of 1 mole of intercalant species (Mg). Thus, x in the equation in **Figure 2c** is the x in $Mg_xMn_2O_4$. At dilute concentrations of mobile ions, the interactions between

the ions are quasi-ideal and Θ approaches 1, at which μ can be written as $\mu = \mu_0 + k_B T \ln(x)$, where μ_0 is the reference chemical potential. At higher concentrations of the migrating ion, where the interactions between the multivalent ions are no longer negligible, Θ deviates from unity.

D_J in the jump diffusivity equation in **Figure 2d** captures the kinetics of random walk motion (see the inset at the top right of **Figure 2**) of diffusing ions and can be written in terms of ionic displacements, $r_i(t)$, of a diffusing atom i after time t, the number of mobile species (normalized per formula unit) N, and the dimensionality d of the diffusion process (i.e., 1D, 2D, or 3D). d is directly related to the topology of ionic migration in the solid of interest. For example, in layered $LiCoO_2$, Li ions move in a 2D lattice, and therefore d is 2, while in spinel-$MgMn_2O_4$, Mg can move in all three directions and d is 3. The term $[\sum_i r_i(t)]^2$ in the jump diffusivity equation in **Figure 2d** can be interpreted as the mean squared displacement (MSD) of the center of mass of all mobile ions in the solid. Importantly, D_J captures all the cross-correlations among the individual atomic migrations that take place, resulting in macroscopic diffusion (52). Thus, D_J is directly related to the conductivity (σ) through the Nernst-Einstein equation (**Figure 2e**). This relationship is explained in detail in Section 3.2.

Random walk motion can also be quantified without explicitly including cross-correlation effects via the tracer diffusion coefficient (D^*) in the equation in **Figure 2f**. D^* tracks the net squared displacement of individual migrating atoms instead of the center of mass. The ratio of D^* to D_J is defined as Haven's ratio (H_R), which is 1 in the absence of ion–ion cross-correlations and becomes appreciably less than 1 in regimes of nondilute diffusion carriers (i.e., significant cross-correlations) (53). Thus, H_R quantifies the extent to which individual atomic migration events that occur sequentially or in parallel contribute to the net movement of mass in a given framework. Also, D^* is proportional to the correlation factor $f = \frac{\langle \Delta R^2 \rangle}{n \Delta r^2}$, where ΔR is the net displacement of a diffusing atom i after n hops and Δr is the average jumping distance of each migration event. f measures the deviation from a fully random walk of the ionic migration in each system and is different from H_R. Furthermore, as shown in the equation in **Figure 2g**, the chemical diffusivity is proportional to the ratio of the square of the distance traversed by the migrating ions and the time taken for the migration for most steady-state diffusion processes.

While D_J (**Figure 2d**) can be derived from the displacement of the center of mass of the active ions, either theoretically or experimentally, a phenomenological expression of D_J is given in Equation 2, which is based on a microscopic view of atoms hopping across equivalent sites and is motivated by the transition-state theory. Equation 2 connects directly with the expression for σ in Equation 1:

$$D_J = \nu^* a^2 f g x_D \exp\left(-\frac{E_m}{k_B T}\right), \qquad\qquad 2.$$

where ν^* is the vibrational prefactor (which takes into account the atomic vibrations as well as entropic differences between the stable and the transition states), a the hopping distance, f the correlation factor, g the geometric factor (how connected the diffusion channels are), x_D the mole fraction of diffusion carriers, and E_m the migration barrier. Importantly, E_m in Equation 2 is the quantity that determines the pace of ionic diffusion in a host material. Previously, it had been demonstrated that a change of ± 50 meV in E_m can cause an order of magnitude change in the resultant D_J (8, 20).

As shown in **Figure 1b,c**, E_m depends on a variety of factors, including the (in)stability of the stable sites across which diffusion occurs, electrostatic interactions within a structure, coordination effects, size of the transition state, and any associated electron transfer as the cation migrates within the anionic lattice. One example of electron transfer is polaronic motion (54, 55), as observed in a common cathode material for Li-ion batteries, $LiFePO_4$. The motion of Li^+ in $LiFePO_4$ is

Table 1 Various experimental and theoretical techniques used to assess ion transport in solids

	D^*	D_J	D_C	E_m	σ	Time	Space
Experimental techniques							
GITT	N	N	Y	N	N	NA	NA
IS	Y*	Y*	N	Y	Y	$10^{-7}\sim10$ s	$10^{-8}\sim10^{-2}$ m
SS-NMR	Y	Y	N	Y	Y*	$10^{-10}\sim10^{2}$ s	$10^{-11}\sim10^{-7}$ m
Muon Spectroscopy	Y*	Y	N	Y	Y*	$10^{-11}\sim10^{-4}$ s	NA
QENS	Y*	Y	N	Y	Y*	$10^{-14}\sim10^{-9}$ s	$10^{-12}\sim10^{-9}$ m
SIMS	Y	Y*	N	Y	Y*	$10^{-5}\sim10^{3}$ s	NA
Theoretical techniques							
AIMD	Y	N	N	Y*	Y*	ps	$10^{-10}\sim10^{-9}$ m
MD (Classical/ML)	Y	Y	Y*	Y*	Y*	ns	10^{-8} m
NEB	Y*	N	N	Y	N	NA	$10^{-10}\sim10^{-9}$ m
kMC	Y	Y	Y*	Y*	Y*	ms	$10^{-9}\sim10^{-8}$ m

Quantities that can be measured directly (Y), inferred from other analytical methods (Y*) based on observations [e.g., by application of the Nernst-Einstein equation (**Figure 2e**)], and cannot be probed (N) are indicated. The timescale of SS-NMR involves all approaches for ion transport characterization, including temperature-variable SS-NMR, SLR SS-NMR, SAE SS-NMR, and PFG SS-NMR. Abbreviations: AIMD, ab initio molecular dynamics; GITT, galvanostatic intermittent titration technique; IS, impedance spectroscopy; kMC, kinetic Monte Carlo; MD, molecular dynamics; ML, machine learning; NA, not available; NEB, nudged elastic band; PFG, pulse field gradient; QENS, quasi-elastic neutron scattering; SAE, spin-alignment echo; SIMS, secondary ion mass spectrometry; SLR, spin-lattice relaxation; SS-NMR, solid state-nuclear magnetic resonance.

accompanied by a local deformation of the host lattice, which results in the localized trapping of electrons (i.e., polarons), causing a reduction of diffusivity (56). Furthermore, x_D can also affect D_J, particularly in scenarios where the host material forms highly stable ordered configurations of the diffusing species. A notable example is the diffusivity of Li in $LiCoO_2$ (57), where the formation of ordered phases at an intermediate Li concentration significantly reduces D_J.

The physical observables in **Figure 2** (i.e., D_C, D_J, D^*, and σ) can be probed with a few experimental and theoretical techniques. A brief overview of the experimental techniques, such as the galvanostatic intermittent titration technique (GITT), impedance spectroscopy (IS), solid state-nuclear magnetic resonance (SS-NMR), muon spectroscopy, quasi-elastic neutron scattering (QENS), and secondary ion mass spectroscopy (SIMS), is provided in **Table 1**. Note that muon spectroscopy (58–61), QENS (62, 63), and SIMS (64–66) can often provide unique probes to investigate ion transport but require dedicated facilities and specific sample conditions, which cannot always be achieved. On the theoretical side, techniques, such as ab initio molecular dynamics (AIMD), classical or machine learning (ML) potentials–based molecular dynamics (MD), the nudged elastic band (NEB) method, and kinetic Monte Carlo (kMC), are also discussed in **Table 1**. We have also indicated which observables can be inferred directly, estimated indirectly, or cannot be inferred for each technique in **Table 1**.

3. EXPERIMENTAL ASSESSMENT OF MAGNESIUM TRANSPORT IN MATERIALS

In this section, we introduce techniques to measure σ (Section 3.1) and D_J (Sections 3.2 and 3.3). Subsequently, in Section 3.4 we discuss the commonly used GITT to measure D_C for electrode materials and elaborate the key differences between chemical and jump diffusion coefficients. Finally, in Section 3.5 we discuss structural characterization techniques that can be used to relate structural features to ion transport.

3.1. Alternate Current Impedance Spectroscopy

Alternate current impedance spectroscopy (AC-IS) is widely used to characterize macroscopic transport of solid-state ionic conductors, including both ionic and electronic conductivity. In a typical AC-IS measurement, a small-amplitude sinusoidal voltage $E(t)$ (or current) is applied to the sample and the corresponding current output $j(t)$ (or voltage) is recorded. The ratio between these two parameters is a complex quantity, namely the impedance:

$$Z(t) = \frac{E(t)}{j(t)}.$$

3.

Impedance measurements can cover approximately ten orders of magnitude in the frequency domain (MHz to mHz), which makes it possible, albeit sometimes challenging, to trace different transport events at different timescales.

A typical impedance representation is the Nyquist plot (67). Since solid-state ionic conductors are often polycrystalline, ion transport can occur within bulk crystals as well as across grain boundaries, leading to distinct features in the Nyquist plot. Thus, for solid-state electrolytes, the Nyquist plot normally includes one or more semicircles in the high-to-medium-frequency domain and a linear tail—the Warburg response—in the low-frequency domain (**Figure 3a**). The linear tail (Warburg) is caused by the usage of ion-blocking electrodes.

The interpretation of Nyquist plots is achieved by fitting the measured data with an appropriate, physically realistic equivalent circuit, where each semicircle is usually represented with one or more resistor and capacitor (RC) elements (**Figure 3a**). The linear tail (with an ideal slope of 45°) is typically modeled by a Warburg impedance element reflecting the mass transfer process at the blocking electrode. Once a reliable equivalent circuit model for AC-IS is obtained, σ can be calculated by Equation 4,
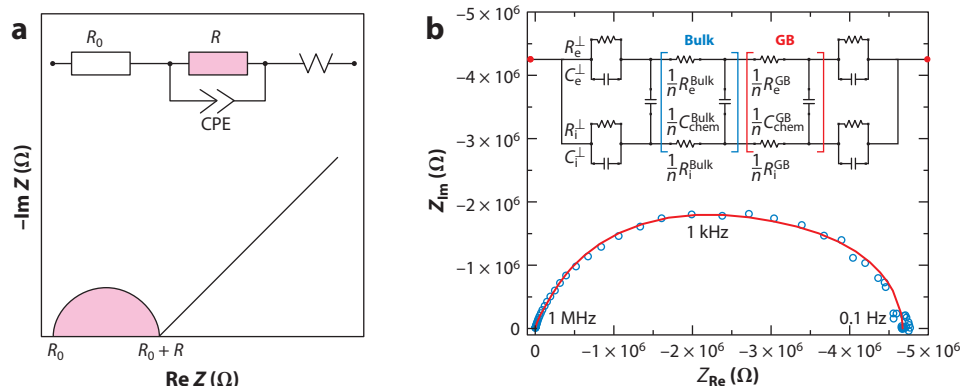
$$\sigma = \frac{L}{RS},$$

4.

Figure 3

(*a*) Typical Nyquist plot of solid-state ionic conductors using ion-blocking electrodes, with the equivalent circuit shown in the inset. The semicircle region in the Nyquist plot represents the ion transport process, the impedance value of which can be estimated based on the resistance value R (*pink*) of the equivalent circuit in the inset. (*b*) Experimental impedance spectra of Ta/MgSc$_2$Se$_4$/Ta at 298 K and the equivalent circuit used in fitting the impedance data (*inset*). The experimental data and fitting result are represented with open circles and a solid line, respectively. The equivalent circuit uses two Jamnik–Maier elements, which separate the bulk and GB contribution of ion transport. Abbreviations: CPE, constant phase element; GB, grain boundary; Im, imaginary; Re, real. Figure adapted with permission from Reference 46.

where L is the thickness of the pellet (i.e., ionic conductor), S is the contact area between the ionic conductor and the ion-blocking electrode, and R is the resistance of ion transport in the conductor (bulk, grain boundary, or both). For instance, using the equivalent circuit with two RC elements in series, the bulk and grain boundary contributions to the total ionic conductivity of $Mg_{0.5}Si_2(PO_4)_3$ (68), which is a typical Na super ionic conductor (NASICON) (69), were determined to be ~5.74×10^{-5} S/cm and ~2.69×10^{-6} S/cm at room temperature, respectively, suggesting an order of magnitude difference in the bulk and grain boundary conductivities.

Nevertheless, it is not always straightforward to separate the bulk and grain boundary contributions when their respective conductivities are similar. For example, Anuar et al. (70) used IS to determine the ionic conductivity of NASICON-$Mg_{0.5}Zr_2(PO_4)_3$, where only one semicircle was observed, thus impeding the separation of bulk and grain boundary effects. A microcontact impedance measurement using a microelectrode has been suggested to unambiguously separate the bulk and grain boundary contributions (71, 72), where the microelectrode (with a diameter of approximately a few microns) can establish contact with a single crystalline domain within a polycrystalline sample. This allows the determination of only bulk ionic conductivity, excluding the effect of grain boundaries. However, performing such microelectrode AC-IS measurements requires sophisticated fabrication techniques and dedicated equipment, such as the preparation of a single-crystal sample.

An ideal solid electrolyte should possess high ionic conductivity (σ_i) and negligible electronic conductivity (σ_e). However, not all solid electrolytes meet these criteria, and IS can be used to assess the relative magnitudes of σ_i and σ_e in such materials (46, 48). For example, the AC-IS response of spinel-$MgSc_2Se_4$, as shown in **Figure 3b**, is characteristic of a mixed (ionic + electronic) conductor (46). Notably, the IS shows a depressed semicircle without a linear tail, although an ion-blocking electrode of Ta metal was used. This peculiar spectrum was modeled by two Jamnik–Maier circuit elements (inset in **Figure 3b**) (73), and σ_i was estimated to be ~0.1 mS/cm at room temperature (46), which is similar to swift Li and Na ionic conductors (74). However, σ_e in spinel-$MgSc_2Se_4$ is relatively large, estimated to be ~4×10^{-4} the magnitude of σ_i, which is significantly higher than the 10^{-8} to 10^{-6} typically required for solid electrolytes. Thus, $MgSc_2Se_4$ is not applicable as a solid-state electrolyte for Mg batteries. While compositional tuning has been proposed to reduce the σ_e of $MgSc_2Se_4$ (47, 48), conclusive experimental evidence of suppressing σ_e does not yet exist (48).

Following the Arrhenius relation of Equation 1, we know that σ is a temperature-dependent quantity. $\ln(\sigma T)$ linearly scales with $1,000/T$ with a slope of E_m. However, we note that $\ln(\sigma)$, rather than $\ln(\sigma T)$, is often plotted against $1,000/T$ in the literature. Although the linear correlation of $\ln(\sigma)$ with $1,000/T$ approximately holds, the extracted E_m is typically underestimated (75). In addition, there are cases where $\ln(\sigma)$ exhibits a change in slope with temperature. For instance, we often observe a change in slope in a $\ln(\sigma)$ versus $1,000/T$ plot at ~180°C in NASICON Mg conductors (70, 76, 77). Specifically, the E_m of $Mg_{0.5}Zr_2P_3O_{12}$ is ~0.17 eV at high temperatures (180 to 550°C), while only about 0.1 eV at low temperatures (25–180°C) (70). This difference is most likely due to the structural transition from monoclinic to rhombohedral NASICON at 180°C. A computational study of the phase behavior of Na-conducting NASICON, $Na_{1+x}Zr_2Si_xP_{3-x}O_{12}$ (69, 78), also indicated that a monoclinic to rhombohedral phase transition can occur at elevated temperatures. We note, however, that the activation energy in NASICON-$Mg_{0.5}Zr_2P_3O_{12}$ is surprisingly small (63), even lower than that of typical Li superionic conductors [e.g., ~0.27 eV for $Li_{10}GeP_2S_{12}$ (79) and ~0.45 eV for $Li_{6.5}La_3Zr_{1.5}Ta_{0.5}O_{12}$ (80)]. More investigations are needed to fully validate and understand the cause of this observed low activation energy.

3.2. Solid State–Nuclear Magnetic Resonance Spectroscopy

SS-NMR spectroscopy can probe ion dynamics at different time and length scales than AC-IS, as shown in **Table 1**. SS-NMR relaxometry, including spin-lattice relaxation (SLR) (T_1, $T_{1\rho}$) and spin-spin relaxation (SSR) (T_2) measurements, can directly probe ion migration events at a few angstroms and at timescales ranging from 10^{-10} s to 10^{-3} s (75). This method can also be used to study correlation effects during ion transport according to the Bloembergen-Purcell-Pound (BPP) model (81).

In SS-NMR, the motion of the nuclei can significantly affect the NMR line shape. At low temperatures, when the motion of nuclei is slow, the SS-NMR peaks exhibit pronounced anisotropy, which is due to specific interactions that are usually present in solids, including dipolar and/or quadrupolar coupling interactions, chemical shift anisotropy, and $\mathcal{J}$-coupling. The strength of these NMR interactions can be expressed in terms of frequency (e.g., kHz or MHz). As temperature increases, the motion of nuclei is enhanced. When the rate of nuclei motion is similar to the strength of the NMR interactions, substantial line narrowing will be observed. If we define the onset temperature of NMR peak narrowing as T_c, E_m, corresponding to the underlying atomic motion, can be estimated using the Waugh and Fedin relation of Equation 5,

$$E_m = 1.617 \times 10^{-3} T_c. \qquad 5.$$

As shown in **Figure 4a** for spinel-MgSc$_2$Se$_4$, the full width at half maximum of the SS-NMR peak at approximately 53.3 ppm showed a line narrowing between 240 K and 283 K, demonstrating the presence of fast local Mg motion within the spinel structure (46). By setting $T_c = 270$ K and following Equation 5, E_m for Mg migration is calculated to be ~0.388 eV.

According to the BPP model (81), the SLR rate R_1 (or $1/T_1$) and temperature can be mathematically related using Equations 6 and 7,

$$R_1 \propto \exp\left(\frac{E_{a,\text{low}}}{k_B T}\right)(T \ll T_{\text{max}}), \qquad 6.$$
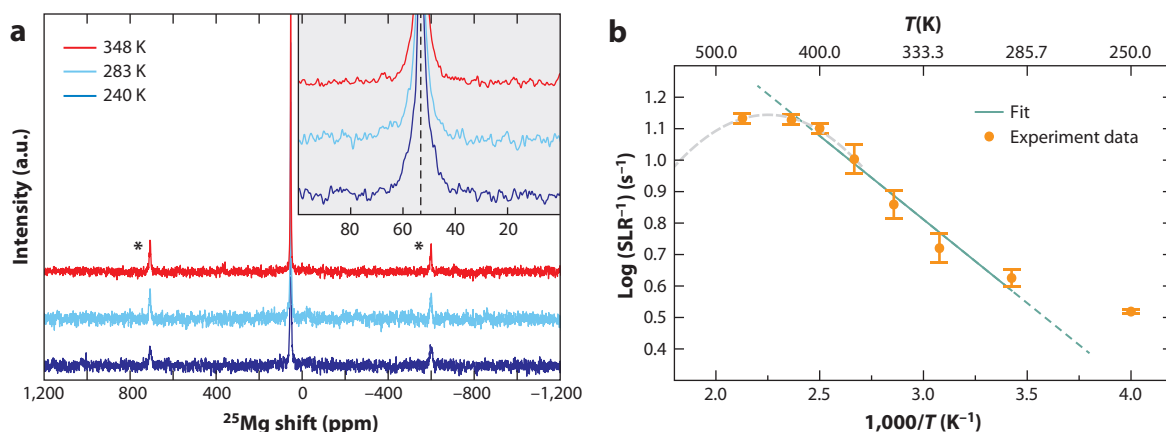

Figure 4

Characterization of Mg ion transport in spinel-MgSc$_2$Se$_4$ via (*a*) variable-temperature ^{25}Mg SS-NMR and (*b*) ^{25}Mg SLR SS-NMR. The green solid line is the Arrhenius fitting result of experimental data, the green dashed line was the deviation of experiment data (*orange dots*) from the fitting result, and the gray dashed curve mimics the expected inverse SLR maxima versus the experimental data. Abbreviations: NMR, nuclear magnetic resonance; SLR, spin-lattice relaxation; SS, solid state. Figure adapted with permission from Reference 46.

$$R_1 \propto \omega_0^\beta \exp\left(-\frac{E_{a,\text{high}}}{k_B T}\right)(T \gg T_{\text{max}}),\qquad\qquad 7.$$

where ω_0 is the Larmor frequency and β, whose value ranges from 1 to 2, is used to describe the asymmetry of the SLR versus the $1{,}000/T$ curve. When $\beta = 2$, ion transport is considered not correlated, while for values of β deviating from 2 and approaching 1, ion transport is considered correlated. Typically, R_1 increases as temperature increases and reaches its maximum when the temperature is raised to T_{max}, beyond which R_1 begins to decrease. The maximum rate R_1 at T_{max} is theoretically the jump rate τ^{-1}, which follows the relation $\omega_0\tau \approx 1$. Therefore, the jump diffusion coefficient D_J can be calculated via the Einstein-Smoluchowski equation (Equation 8),

$$D_J = \frac{a^2}{6\tau},\qquad\qquad 8.$$

where a is the jump distance between two neighboring crystallographic sites. As an example, Canepa et al. (46) used ^{25}Mg SLR SS-NMR to probe Mg^{2+} diffusion in $MgSc_2Se_4$, as shown in **Figure 4b**. Due to the limited temperature range, a complete SLR SS-NMR curve with an obvious R_1 maximum could not be clearly observed. With the assumption that the maximum of R_1 appears at $\sim$450 K, the local Mg jump rate τ extracted from SLR SS-NMR is 1.15×10^8 s^{-1}. In turn, via $\omega_0\tau \approx 1$ ($\omega_0/2\pi = 18.37$ MHz), D_J can be calculated to be $\sim$4.53 $\times 10^{-8}$ cm^{-2} s^{-1} at 450 K via Equation 8. Importantly, E_m fitted with the BPP model (green line in **Figure 4b**) is $\sim$0.37 $\pm$ 0.09 eV, which is consistent with E_m from the line width narrowing analysis (0.388 eV; see discussion above).

Microscopic diffusion can also be probed using SLR SS-NMR in the rotating framework, where the SLR rate in rotation frame of reference $R_{1\rho}$ ($1/T_{1\rho}$) is measured. In this method, due to the lower Larmor frequency ω_1 (usually tens of kHz), slower Mg^{2+} motion can be detected better as compared with the SLR SS-NMR measurement. The jump rate can be obtained via $\omega_1\tau \approx 0.5$. Thus, combining both T_1 and $T_{1\rho}$ measurements, ion transport with jump rates ranging from 10^4 to 10^{11} s^{-1} can be measured using SS-NMR (82–84).

3.3. Quasi-Elastic Neutron Scattering

QENS is a powerful technique to investigate ion motion in condensed matter with timescales ranging from 10^{-14} s to 10^{-9} s (75). Motion at such timescales can result in characteristic broadening of the elastic peak at zero energy transfer (i.e., $\Delta E = 0$ meV). The quality of QENS data relies heavily on the incoherent cross section of the element probed (see **Table 2**). Apart from the low natural abundance of ^{25}Mg (10.13%), the incoherent cross sections of ^{24}Mg and ^{25}Mg are

Table 2 Neutron cross sections of Mg and H isotopes

Isotope	Coherent cross section	Incoherent cross section	Scattering cross section	Absorption cross section
Mg	3.631	0.08	3.71	0.063
^{24}Mg	4.03	0.00	4.03	0.05
^{25}Mg	1.65	0.28	1.93	0.19
H	1.7568	80.26	82.02	0.3326
^{1}H	1.7583	80.27	82.03	0.3326
^{2}H	5.592	2.05	7.64	5.19×10^{-4}
^{3}H	2.89	0.14	3.03	0.00

Data is in units of barn, with 1 barn $= 1 \times 10^{-24}$ cm^2. Data from Reference 87.

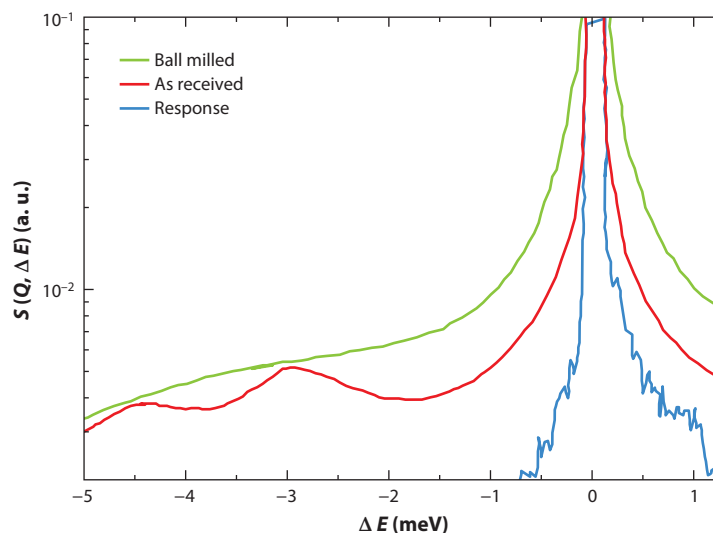**Figure 5**

Mg(BH$_4$)$_2$ in the crystalline γ-phase (as received, *red*) and amorphous phase (ball milled, *green*). $S(Q, \Delta E)$ measured at $\lambda_1 = 5$ Å, $Q = 1.35$ Å^{-1}, and 310 K. The curves show only the fitting results. The blue curve shows the measured resolution function at 3.5 K. Figure adapted and digitized with permission from Reference 86.

0 and 0.28 barns, respectively, which render it challenging to directly probe Mg ion dynamics using QENS. However, QENS spectra are sensitive to hydrogen (H), whose incoherent cross section is 80.26 barns. Therefore, Mg ionic conductors containing H, such as Mg(BH$_4$)$_2$-type conductors (85, 86), can be investigated by QENS by establishing links between anion reorientation and Mg diffusion.

Indeed, Heere et al. (86) suggested a two-orders-of-magnitude increase in ionic conductivity in amorphous γ-Mg(BH$_4$)$_2$ compared with crystalline γ-Mg(BH$_4$)$_2$ on the basis of QENS measurements. The authors attributed the increased ionic conductivity to the increased rotational rate of the BH$_4^-$ group observed in the amorphous phase (versus the corresponding crystalline phase) through QENS. As shown in **Figure 5**, the crystalline γ-Mg(BH$_4$)$_2$ (red curves labeled "as received") showed almost no quasi-elastic scattering around the elastic peak ($\Delta E = 0$ meV) at 310 K, while significant broadening is observed in the amorphous γ-Mg(BH$_4$)$_2$ (green curves labeled "ball milled"). This indicates that the BH$_4^-$ moieties in amorphous γ-Mg(BH$_4$)$_2$ possess higher mobility than those in crystalline γ-Mg(BH$_4$)$_2$. Previously, it has been demonstrated in Li and Na borohydride ion conductors that the Li$^+$ and Na$^+$ ion jumps are strongly correlated with the reorientation of BH$_4^-$ groups (88). Therefore, Heere et al. (86) speculated that the higher ionic conductivity in amorphous Mg(BH$_4$)$_2$ originated from the fast reorientation of BH$_4^-$ groups.

3.4. Galvanostatic Intermittent Titration Technique

GITT, which was first proposed in 1977 by Weppner & Huggins (89), is the most commonly used method to assess D_C (of the equation in **Figure 2b**) in electrode materials. D_C can be affected by diffusion processes within the bulk structure and across grain boundaries, as well as by any applied concentration gradients (or chemical potential differences) at the electrode level.
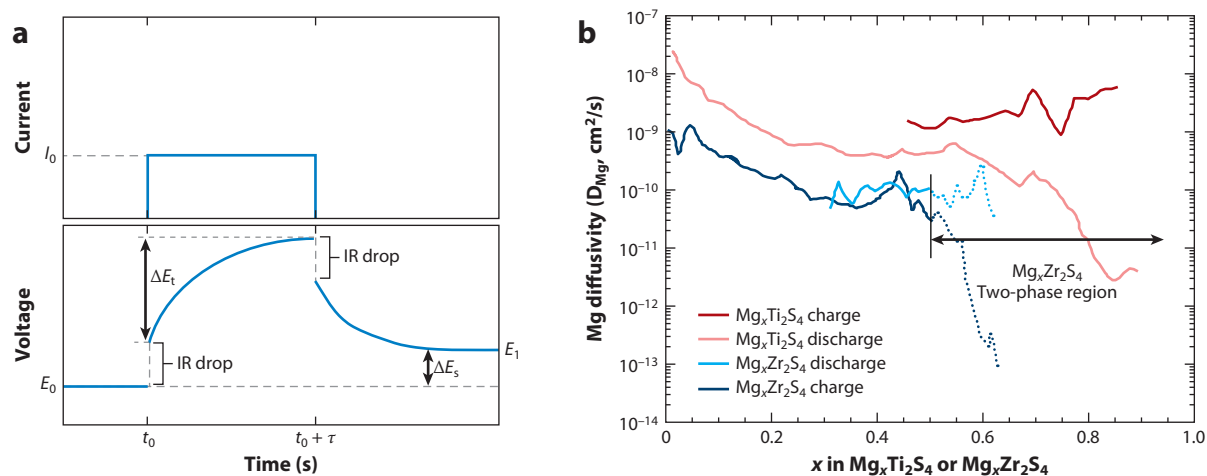
Figure 6

(*a*) Schematic of the GITT working principle using one current pulse. (*b*) Mg ion diffusion coefficients in spinel Ti_2S_4 and Zr_2S_4 measured via GITT at 60°C. $Mg_xZr_2S_4$ formed a second phase as *x* is larger than 0.5 (*dotted lines*), preventing the accurate determination of the Mg diffusion coefficient. Abbreviations: GITT, galvanostatic intermittent titration technique; I, current; R, resistance. Figure adapted with permission from Reference 90; copyright 2017 American Chemical Society.

In GITT measurements, a constant current is applied to the electrode for a defined period and the voltage response is measured and analyzed, as shown in **Figure 6a**. The current causes ions near the electrolyte–electrode interface to diffuse, which produces a concentration gradient at the electrode level and a change in the electrode potential. When the current pulse is removed after time (*t* or τ), the ionic concentration within the electrode reequilibrates because of diffusion, which leads to the electrode potential reaching a new equilibrium value. Therefore, the rate at which the electrode potential relaxes is related to the rate of (chemical) diffusion. Thus, D_C can be calculated at different states of charge in the electrode using Equation 9,

$$D_C = \frac{4}{\pi}\left(\frac{jV_m}{zFS}\right)^2 \left[\frac{\left(\frac{dE}{d\delta}\right)}{\left(\frac{dE}{d\sqrt{t}}\right)}\right]^2 \left(t \ll L^2/D_C\right), \qquad 9.$$

where V_m is the molar volume of electrode material, S is the area of the electrode, F is Faraday's constant, z is the number of electrons, j is the applied current, $\frac{dE}{d\delta}$ is the slope of the coulometric titration curve, $\frac{dE}{d\sqrt{t}}$ is the slope of the voltage change as a function of the square root of the duration time of the current pulse, and L is the sample thickness. If the applied current is small enough, $\frac{dE}{d\sqrt{t}}$ can be considered as linear. Accordingly, Equation 9 can be simplified to Equation 10,

$$D_C = \frac{4}{\pi\tau}\left(\frac{n_m V_m}{S}\right)^2 \left(\frac{\Delta E_s}{\Delta E_t}\right)^2 \left(\tau \ll L^2/D_C\right), \qquad 10.$$

where n_m is the number of moles of the active diffusing ion, ΔE_s is the steady-state potential change caused by the current pulse, and ΔE_t is the potential change during the constant current pulse (see **Figure 6a**).

Previously, Bonnick and colleagues (28, 30) measured the D_C of Mg ions in different spinel structures via GITT (**Figure 6b**). The D_C of Mg^{2+} in Ti_2S_4 at room temperature was measured to be $\sim 10^{-11}$ cm^2/s and $\sim 10^{-12}$ cm^2/s during charge and discharge, respectively, which suggest that the rates of Mg deintercalation and intercalation processes are different (30). Furthermore,

they found that during the discharging process in $Mg_xTi_2S_4$, the Mg D_C decreased sharply for $x > 0.55$, which could be ascribed to the decrease in the number of available Mg intercalation sites (30). Later, the same research group measured the Mg D_C in another spinel, namely Zr_2S_4 (90), which varied within the range of 10^{-10} to $\sim 10^{-9}$ cm^2/s during charge and discharge at $\sim 60°$C. These D_C values are almost two orders of magnitude lower than that of Ti_2S_4 at $\sim 60°$C (10^{-9} to $\sim 10^{-8}$ cm^2/s), which was attributed to the different electronic conductivities of Ti_2S_4 and Zr_2S_4.

3.5. Structural and Mg Ion Transport Properties

Diffraction techniques, such as X-ray diffraction (XRD) and neutron diffraction (ND), are widely used for structural characterizations of crystalline materials. The positions of diffraction peaks depend on the lattice parameters and the space group of the lattice, whereas the intensities of the diffraction peaks rely on their atomic positions, relative occupancies, and thermal displacements.

The thermal displacements obtained from the diffraction analysis can be used to gauge the mobility of ions. It is important to note that an accurate understanding of the crystallographic structure of fast ionic conductors is a prerequisite for relating structural features to ion transport properties. For light elements (e.g., Li), the accurate determination of their atomic positions and thermal displacement requires advanced neutron facilities (91, 92). Kamaya et al. (79) explored the location of Li ions in $Li_{10}GeP_2S_{12}$ by ND. It was revealed that the Li ions were displaced from the 16h and 8f sites toward the interstitial positions between two 16h sites and/or between the 16h and 8f sites. This observation suggested the existence of a one-dimensional conduction pathway along the c-axis of the thio-LISICON structure (79).

Because Mg is heavier than Li, determination of atomic position and thermal displacement can be achieved via laboratory XRD and more accurately by synchrotron X-ray sources, which make the studies of Mg compounds more accessible. However, high-quality diffraction data and in-depth structural analysis of Mg ionic conductors are scarcer than those of Li or Na solid electrolytes. Notably, a comprehensive structural investigation of Mg borates (cathode) by Bo et al. (93) suggests that a detailed study can provide critical insights into the mechanism of Mg diffusion in solids.

To elaborate further, through characterization of a series of thermally demagnesiated $Mg_xFe_{2-x}B_2O_5$ by synchrotron X-ray and time-of-flight ND, the population of Mg at the inner two (M_B) and outer two (M_A) octahedral sites in the ribbon framework can be measured (93). Note that the structure contains four parallel chains of edge-sharing octahedra (two outer orange M_A octahedra and two inner pink M_B octahedra; **Figure 7a**). It was found that Mg is depopulated only from M_B sites, while the M_A sites remained fully occupied during the thermal oxidation process. This is consistent with higher Mg mobility at M_B sites as determined from the analysis of bond valence sum difference maps. In addition, the Mg diffusion in the $Mg_xFe_{2-x}B_2O_5$ framework was also found to be tolerant to the presence of defects on the octahedral sites (**Figure 7a**).

Additionally, an operando XRD study by Yin et al. (94) illustrated the cation migration mechanisms of a spinel $MgCrMnO_4$ cathode. The results revealed that the migration of Mg^{2+} predominantly occurs between the 8a and 16c sites while the occupancy at 16d sites remains unchanged and is accompanied by the migration of inverted Mn (**Figure 7b**). It was also demonstrated that the intercalation/deintercalation of Mg^{2+} is highly reversible in $Mg_{1-x}CrMnO_4$ ($x \leq 1$).

4. THEORETICAL CALCULATIONS OF MAGNESIUM TRANSPORT IN MATERIALS

Figure 8 shows the trade-off between accuracy and scale in commonly used computational approaches to probe Mg^{2+} transport in materials, where the goal of each approach is to determine
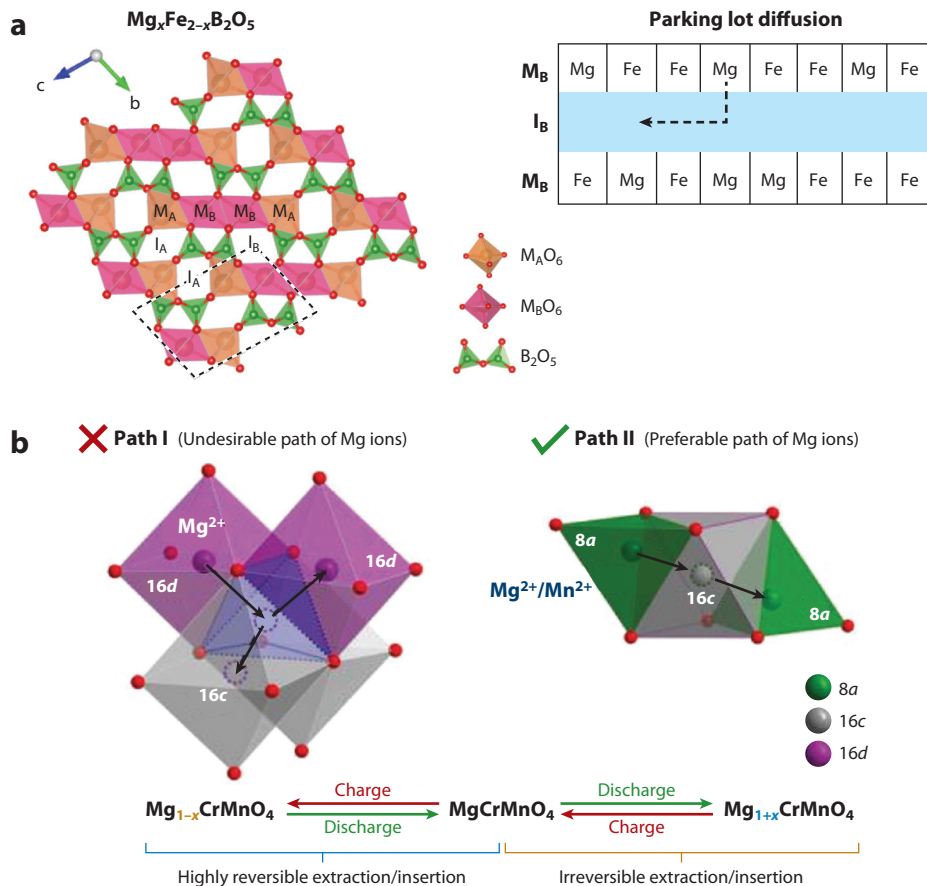
Figure 7

(*a*) Mg diffusion diagram of the $Mg_xFe_{2-x}B_2O_5$ structure. Panel adapted with permission from Reference 93; copyright 2015 American Chemical Society. (*b*) Mg migration pathway in $MgCrMnO_4$. The Mg ion prefers Path II, jumping directly along the tetrahedral site (8*a*)-octahedral site (16*c*)-tetrahedral site (8*a*) path, rather than Path I, where the Mg ion jumps from an octahedral site (16*d*) to another octahedral site (16*c*), crossing a tetrahedral site. Adapted with permission from Reference 94; copyright 2021 American Chemical Society.

the potential energy surface (PES; see inset in **Figure 8**) of a given material system. Currently, two main approaches are in use to estimate Mg mobility in host materials, namely the NEB method coupled with density-functional theory (DFT) (and rarely with kMC) (95–98) and MD simulations (99, 100).

4.1. Molecular Dynamics

In the MD approach, the migration of ions is modeled by solving Newton's equations, which requires the accurate determination of forces acting on atoms at each time step (100). In turn, in each material, the forces in MD are determined by the evolution of the PES with time, with computational cost typically increasing with the level of accuracy required to estimate the PES. Therefore, the approach used to obtain the PES determines the type of MD simulations employed.
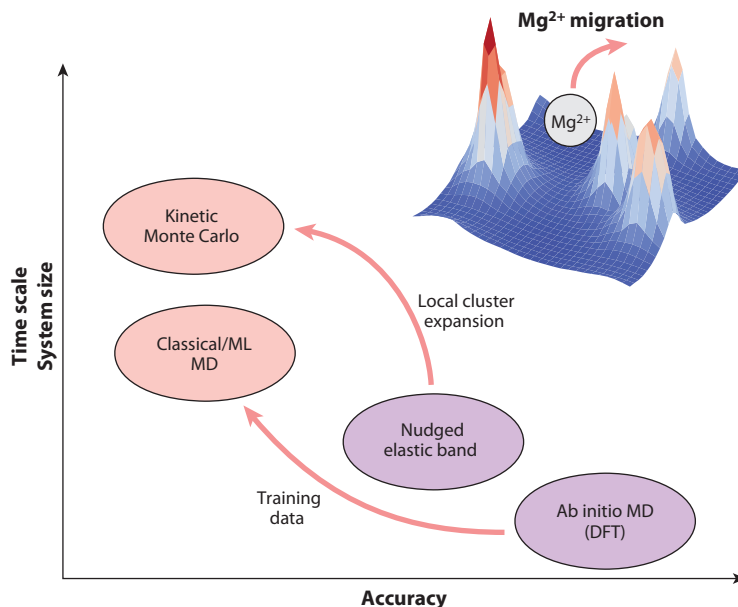
Figure 8

Computational frameworks for the determination of Mg^{2+} transport. Data generated from computationally expensive but accurate first-principles calculations (*purple bubbles*) are used to build models (cluster expansions and/or ML) to perform larger scale and longer simulations via kinetic Monte Carlo and/or classical/ML MD. The inset depicts a potential energy surface schematic. Abbreviations: DFT, density-functional theory; MD, molecular dynamics; ML, machine learning.

AIMD provides a robust, parameter-free evaluation of the PES (and forces), accessed by solving the Schrödinger equation with either the Car–Parrinello method or under the Born–Oppenheimer approximation (100, 101), that has been used to study the diffusion mechanisms in superionic conductor and electrode materials (102, 103). For example, AIMD has recently been used for the prediction of a new Li-ion conductor, namely a quaternary phosphate containing Li and Ge (104). Although highly accurate and transferable, AIMD is still computationally intensive and has poor scalability [$>O(N^3)$] (100). This limits the typical simulations to small system sizes (<1,000 atoms) and short timescales (approximately hundreds of picoseconds; see **Table 1**).

Alternatively, PESs are obtained using parameterized interatomic potentials (IAPs), also referred to as force fields (100, 105). IAPs are often fitted from data obtained from experiments, accurate first-principles calculations, or a mixture of both. The advantage of using force fields is an enormous reduction of the computational time (i.e., larger size and longer simulations) while having a physically interpretable mathematical formalism. However, there are trade-offs (**Figure 8**) between computational cost and accuracy (sampling instances not presented during training), transferability (using IAPs trained on small bulk data sets on larger surface-containing systems), and availability (especially for new materials with exotic properties) in employing IAPs.

Recently, ML approaches have been actively sought for developing effective IAPs, which are commonly referred to as machine learning potentials (MLPs). Modern MLPs are based on the formalism of force-matching developed by Ercolessi & Adams (106), which fits an IAP to reproduce DFT-calculated forces. Notably, MLPs differ from traditional force fields in three aspects: (*a*) the amount of training data required, (*b*) the accuracy of the PES, and (*c*) physical

interpretability. Typically, an MLP is fitted to a large training set, generally a database of thousands of DFT (or similar) calculations (and/or experimental data). Various regression or modeling techniques, such as linear regression, Gaussian process regression, neural network–based regression, and kernel ridge regression, are subsequently applied to describe the PES as a function of elemental, structural, and/or atomic configurational descriptors. Since MLPs utilize a larger and more diverse training set to fit to complex mathematical functions than traditional force fields, they are in general more accurate but with a higher computational cost (107, 108) and lower physical interpretability (109, 110). Some of the popular approaches in developing MLPs are the moment tensor potentials (111, 112), Gaussian approximation potentials (113), spectral neighbor analysis potentials (114), and neural network potentials (108, 115).

4.2. Nudged Elastic Band

An alternative theoretical framework to study ionic mobility is by calculating the E_m associated with atomic hops in a host lattice using DFT-based NEB (95, 96). In this framework, a number of intermediate positions representing the migrating species (images) are connected to form an elastic band, which acts as an initial guess for the minimum energy path (MEP) in a given structure (95). Each image is spaced from its neighbors by adding fictitious spring forces that maintain the shape of the band, resulting in a constrained optimization to obtain the MEP. The difference between the highest and the lowest energy images along the converged MEP denotes the E_m.

Although it is possible to perform NEB calculations with IAPs, most NEB calculations nowadays rely on DFT for the estimation of total energies and forces on atoms, which imposes constraints on the size of the system, number of images used, and the range of different migration events considered. Notwithstanding the time-consuming nature of NEB calculations, intelligent strategies have been proposed to accelerate their preparation and execution (43, 116–118).

4.3. Kinetic Monte Carlo

Since ionic diffusion is a stochastic process involving a large number of individual atomic migration events, either sequentially or in parallel, ensemble-sampling techniques such as kMC can be used instead of MD. Based on the known E_m of different local migration events (either from experimental data or calculated using DFT-NEB), kMC can be used to model the large time and length scales, respectively, of ionic diffusion, yielding quantities including D_J, D^*, and σ. Starting from a known structure (usually obtained from canonical or grand-canonical MC simulations), kMC involves two distinct steps: selecting a migration event to occur and updating the physical time (97, 119). For selecting the migration event, the frequency associated with a given hop (Γ), based on transition state theory, is used as in Equation 11,

$$\Gamma = \nu^* e^{\left(-\frac{E_m}{k_B T}\right)},$$ 11.

where ν^* is the vibrational prefactor (in s^{-1}). Note that E_m in Equation 11 needs to be estimated for a variety of local environments for kMC simulations to be accurate. In practical implementations of kMC, a local cluster expansion (53, 120, 121) is often used to extrapolate E_m to local environments that are not calculated explicitly using NEB. Additionally, local cluster expansions are typically fitted to calculated kinetically resolved activation barriers (97), which removes any directional dependence in E_m due to the asymmetry of the MEP between initial and final states of a given hop.

4.4. Theory in Practice

Having discussed several approaches to assess the mobility of Mg ions in materials, we now review some recent implementations of these techniques. Using DFT-NEB calculations, Rong et al. (122) investigated mobility of MV ions (Mg^{2+}, Zn^{2+}, Ca^{2+}, and Al^{3+}) in typical compact cathode host materials, such as spinel Mn_2O_4, olivine $FePO_4$, layered NiO_2, and δ-V_2O_5. Importantly, the authors isolated the chemical and structural factors (see below) required for facile migration of Mg^{2+} in compact host structures, which have been applied and extended to the interpretation of experimental and theoretical investigations of Mg ions in spinel oxides and chalcogenides (28–30, 32, 38, 39, 42, 90, 94). For example, Canepa et al. (46), using DFT-NEB (and supplemented by AIMD) calculations, calculated E_m for Mg in a large set of spinel materials, as shown in **Figure 9**. Selected migration barriers in **Figure 9** were also corroborated by SS-NMR and AC-IS measurements (123). Recently Koettgen et al. (124) have extended the results presented in **Figure 9** to rare-earth-containing Mg spinels.

Assuming the absence of spinel inversion (38), the E_m values shown in **Figure 9** are associated with the typical migration mechanism of tetrahedral → octahedral → tetrahedral (tet-oct-tet) (22, 28, 31, 32, 38, 46, 116, 124), and several design rules can be extracted:

1. Overall, E_m is inversely proportional to the volume per anion in spinels, with E_m following the order $O^{2-} > S^{2-} > Se^{2-} > Te^{2-}$ (oxides not shown in **Figure 9**). Apart from increasing anion size, moving down the group of the chalcogenides also increases the electric polarizability of the anion, which is the ability of the positive charge of a nearby cation to deform the anion's electronic charge density. Increasing anion polarizability enables facile cation diffusion because the anionic charge cloud can more easily deform with cationic motion. However, the nature of the non-Mg cation in the spinel also influences the electronic
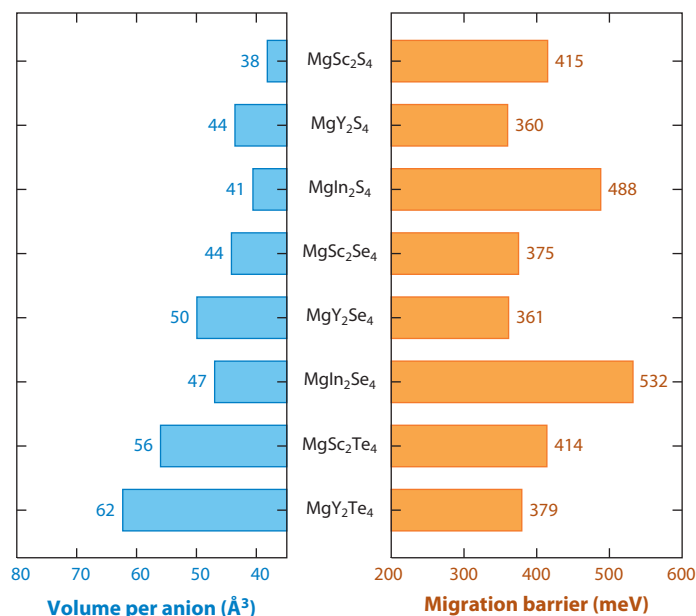

Figure 9

Density-function theory-nudged elastic band Mg migration barriers in MgT_2X_4 spinel frameworks, with T = Sc, Y, and In and X = S, Se, and Te.

structure (125) and in turn the Mg motion in the spinel, as highlighted by higher barriers in some tellurides (e.g., $MgSc_2Te_4$; **Figure 9**) compared with the corresponding selenide (e.g., $MgSc_2Se_4$).

2. Rong, Liu, and colleagues (22, 122) have also indicated that a reduction of E_m for Mg can be attained by selecting anion frameworks where the stable site for Mg displays an unfavorable coordination (i.e., a higher-energy stable site) and the transition state has a more favorable coordination (i.e., a lower-energy transition site). For example, spinel frameworks can exhibit low E_m for Mg since the stable (transition) state exhibits an unfavorable (favorable) coordination of four (6), following a tet-oct-tet pathway (8, 28, 30, 38).

3. A flattening of the MEP can be achieved by reducing changes in the coordination number of Mg^{2+} during its migration (21, 122).

The identification of protective coating materials, where facile Mg transport is important, that can stabilize the electrode–electrolyte interface remains an active area of research in Mg and MV batteries (43, 44). Recently, Chen et al. (43) performed extensive DFT-NEB calculations to identify stable coating materials enabling facile migration of Mg ions. Using a simple steady-state diffusion model containing three variables, namely, the thickness of the coating material, the temperature of operation, and the rate of (dis)charge, the authors derived two limiting mobility criteria: (*a*) maximum $E_m \sim 600$ meV for a 50-nm-thick coating at 25°C and at 10*C* (high rate) and (*b*) maximum $E_m \sim 980$ meV for a 1-nm-thick coating at 60°C and *C*/2 (low rate) (43). These limiting criteria were then used to identify promising materials, as depicted in **Figure 10**.
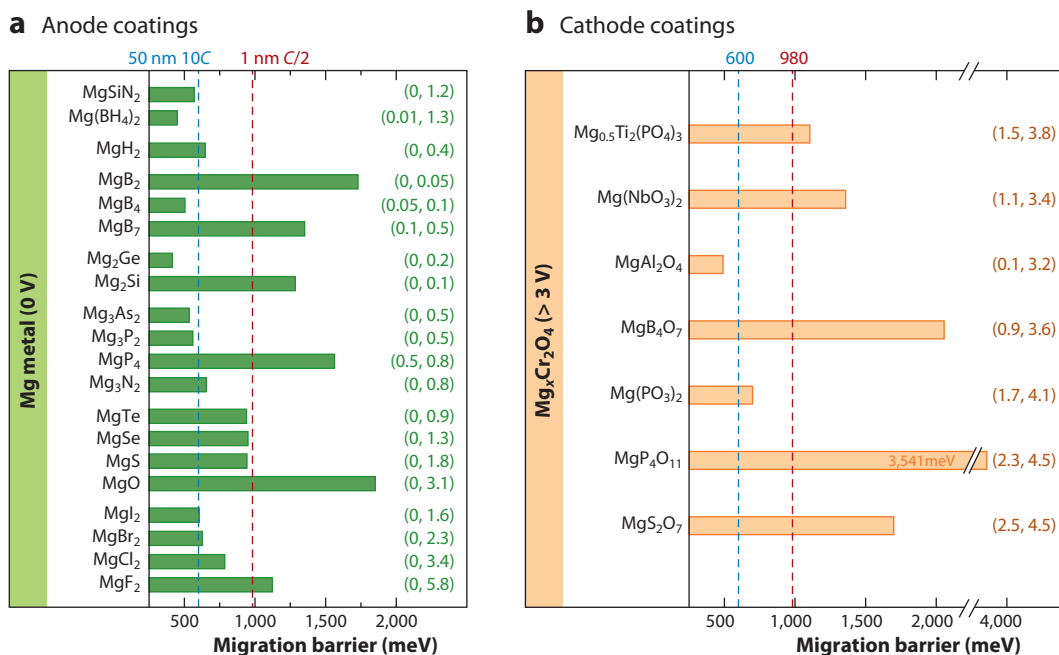

Figure 10

Density-functional theory-nudged elastic band E_m for anode (*left*) and cathode (*right*) coating candidates. Dotted vertical lines indicate strict (~600 meV, *blue*) and lenient (~980 meV, *red*) mobility criteria. Numbers in parentheses show the reductive and oxidative electrochemical stability limits, in V versus Mg metals. Figure adapted from Reference 44; copyright 2019 American Chemical Society.

Employing the strict mobility criterion (maximum $E_m \sim 600$ meV in **Figure 10**), several coating materials with good Mg E_m were identified, namely $MgSiN_2$, MgB_4, Mg_2Ge, Mg_3As_2, Mg_3P_2, and $MgAl_2O_4$. If a lenient criterion is adopted (maximum $E_m \sim 980$ meV), more materials appear suitable as coatings, including MgH_2, Mg_3N_2, MgTe, MgSe, MgS, MgI_2, $MgBr_2$, $MgCl_2$, and $Mg(PO_3)_2$. Out of all the coating candidates, $MgAl_2O_4$ and $Mg(PO_3)_2$ should be compatible with oxide cathodes (>3 V versus Mg), while $MgSiN_2$, MgS, MgSe, $MgBr_2$, and MgI_2 should be compatible with the Mg metal anode and exhibit a reasonable range of electrochemical stability (>1 V versus Mg). The experimental realization of such coating candidates remains to be seen.

5. CHALLENGES ASSOCIATED WITH EVALUATING MAGNESIUM ION TRANSPORT

In the previous sections, we have reviewed specific experimental and computational techniques to study the transport of Mg (and other MV) ions in crystalline hosts. In this section, we cover some of the challenges that remain in both experimental and computational methods to accurately quantify Mg mobility.

5.1. Experiments

As discussed in Section 3.1 and **Table 1**, AC-IS can be used to determine σ in a compound, though a few difficulties remain, especially for solid-state electrolytes:

- An ideal solid-state electrolyte is required to have high σ_i and negligible σ_e. Recently, the σ_e values of solid-state electrolytes have been suggested to greatly affect the formation of metal dendrites (126), and high σ_e was also observed in several Mg ion conductors (46, 48). However, decoupling σ_i and σ_e via AC-IS alone is not trivial. Therefore, complementary methods are required to quantify σ_e; direct current polarization, Tubandt direct current, and Hebb–Wagner methods can be used (127).
- To accurately determine σ_i, the ion-blocking electrode should be inert and stable against the ion (e.g., Mg) whose conductivity is being investigated. However, finding an ideal ion-blocking electrode for Mg solid-state conductors is not as trivial as for Li and Na, where several working examples exist. For example, when using Ag as the ion-blocking electrode, the impedance of an $Ag/MgSc_2Se_4/Ag$ cell increases from approximately 300 to 400 kΩ after 40 minutes (46), indicating the instability between the electrolyte and electrodes. Even when Pt was used as an ion-blocking electrode, the impedance still dramatically increased (46).
- σ_i and E_m measured by AC-IS can be very sensitive to sample preparation and measurement conditions. Notably, Ohno et al. (128) conducted a systematic study to estimate the uncertainty of interlaboratory reproducibility of σ_i and E_m by comparing AC-IS-measured σ_i and E_m of Li argyrodites of identical composition and structure, made via the same synthetic route but in different laboratories. Importantly, the comparison showed that the standard deviations of σ_i and E_m were 35–50% and 5–15%, respectively. The large uncertainties in measured σ_i and E_m indicate the necessity of more rigorous measurement conditions, such as a well-controlled environment (H_2O and O_2 content), a consistent sample history, and multiple repeats.

A few recent publications (e.g., 129) that have calculated σ_i and E_m using AC-IS in Mg-containing compounds have reported that a low E_m does not necessarily result in a low σ (and vice versa), in contradiction to Equation 1. Gao et al. (129) have attributed this anomaly to the Meyer-Neldel energy (130), which quantifies the variation of σ_o with E_m. Physically, Meyer-Neldel

energy is caused by a distribution of E_m in a given material, which in turn can be caused by chemical inhomogeneity and/or strong defect–defect interactions (130). In other words, the entropy of a migration event (i.e., the number of different ways a migration event can occur) has a strong dependence on E_m (i.e., the energy required for the migration event), resulting in a dependence of σ_o on E_m. However, Meyer-Neldel energy can spuriously be thought to contribute to a given structure due to a wrong fit of the $\ln(\sigma T)$ versus $1{,}000/T$ curve or to performing the AC-IS at temperatures close to a phase transition of the underlying material. Hence, complementary experiments (see **Table 1**) to obtain either σ or D_J will aid in identifying and validating any effects from Meyer-Neldel energy. Nevertheless, a strong dependence of σ_o on E_m can, in some cases, have a beneficial effect on transport properties (129).

The use of ^{25}Mg NMR to determine local structures and ion dynamics in solids is relatively scarce in the literature compared with Li (84, 131), O (132, 133), and H (37, 134, 135). The challenges of obtaining high-quality ^{25}Mg NMR data are twofold:

- ^{25}Mg is a 5/2 quadrupolar nucleus exhibiting a significantly large quadrupole moment, Q. On the one hand, this suggests that ^{25}Mg is a very sensitive probe of the local Mg environment. On the other hand, Q of ^{25}Mg (0.22×10^{28} Q/m^2) (136) is 248 times larger than that of ^{6}Li and 5 times larger than that of ^{7}Li (136), which causes substantial broadening of NMR peaks and makes it difficult to obtain high-quality ^{25}Mg NMR data with high resolution.

- The small gyromagnetic ratio [$\gamma = -1.64 \times 10^7$ rad/(s·T)] and low natural abundance of 10.1% of the ^{25}Mg isotope impedes obtaining NMR spectra with a high signal-to-noise ratio. The receptivity, a parameter to measure how easy it is to acquire the NMR spectrum of one nucleus, is determined by the product of the natural abundance (%) and the NMR sensitivity [$|\gamma^3|I(I+1)$, where I is the nuclear spin angular momentum]. Thus, the receptivity of ^{25}Mg is only ~0.92% and ~30% of ^{7}Li and ^{6}Li nuclei, respectively, indicating the increased difficulty in acquiring high-quality NMR spectra for Mg. Magic angle spinning techniques (137) can overcome some of the drawbacks associated with solid-state ^{25}Mg NMR (46, 138). However, more work is required in terms of instrument and methodology improvement to increase the quality of ^{25}Mg NMR data.

5.2. Theory

While the identification of promising Mg (and other MV) ionic conductors can benefit enormously from inexpensive and fast computational screening (45), a fundamental understanding of the chemical and structural factors affecting the transport properties is imperative to accelerate materials design. While computational modeling has provided valuable insights so far (as discussed in Section 3.4), more work is required to further improve such insights, generalize them to other MV ions, and eventually design materials with superior Mg (and MV) ionic conductivity. Here, we summarize some of the challenges faced in theoretical practices.

- AIMD simulations are de facto the preferred methodology for probing Li transport in electrolytes and electrodes. However, AIMD is computationally expensive, with nonnegligible constraints on the maximum time and length scale of the diffusion probed during each simulation. Therefore, the accumulation of sufficiently useful statistics with AIMD simulations is challenged by cases of poor ionic migration, which is common in several Mg (or MV) conductors (46). Thus, the computational cost-to-accuracy trade-off is not favorable for AIMD in most Mg (or MV) systems.

- The force fields and/or MLPs used in classical MD are computationally more accessible when compared with AIMD, but they exhibit issues of accuracy in the case of force fields and lack of descriptive physics in the case of MLPs. Both classes of IAPs share the issue of low transferability between different material systems. However, new advancements in MLPs may address the transferability issue in the future.

- NEB calculations are a valuable alternative to MD for calculating transport properties since they directly evaluate E_m. However, high-throughput DFT-NEB calculations remain difficult in their preparation, execution, and convergence. Although attempts have been made to improve the NEB convergence and runtime speed by providing a better initial MEP, substantial improvements are still required to practically implement high-throughput NEB (116, 117). Furthermore, the sensitivity of the exchange and correlation functionals in predicting the migration barriers from NEB remains to be tested and needs more systematic studies (139–141).

- Since ion transport is thermally activated, it becomes crucial to account for entropic effects. Although DFT calculations have been reliable, new models of Mg (or MV) transport need to incorporate statistical mechanics to account for configurational and vibrational entropic effects. An example of including entropic effects is using a local cluster expansion in conjunction with kMC simulations, where E_m is calculated as a function of chemical environment (97). Nevertheless, developing such models is challenging given computational costs and convergence difficulties.

- Apart from the challenges at the electronic and atomic levels of calculations mentioned above, there is an enormous gap in researchers' ability to simulate materials with chemical accuracy at the mesoscale, wherein surface and interfacial effects can be better described. So far, there is limited understanding of the types and rates of chemical reactions and ion transport across electrode–electrolyte interfaces (142–144). While MLPs show promise for improving accuracy at large system sizes and hence improving fundamental understanding of the processes at interfaces, they are still an order of magnitude (or worse) slower than techniques using force fields, such as the embedded atom method (145, 146). Hence, integrated computational materials science approaches, where electronic- and atomic-scale calculations are combined with appropriate mesoscale frameworks while ensuring accuracy loss is minimized, may be of help in simulating interfaces.

6. FUTURE DIRECTIONS AND OUTLOOK

In this review, after providing a brief overview of the fundamentals of ionic mobility, we discuss the experimental and theoretical techniques that are typically used for probing ion transport in materials and their applications for studying Mg transport in a variety of host frameworks. We also summarize the advantages and disadvantages of different techniques, what specific transport quantities a technique can measure (or probe), and a set of general challenges that remain across techniques in quantifying Mg (and MV) mobility in materials. We hope that this review provides a good foundation for future studies to better quantify ionic transport, especially that involving Mg and other MV ions, thereby leading to the development of practical Mg (or MV) batteries. Having said that, the following are some of the directions where we believe that immediate follow-up research will be useful.

The current set of design rules, as proposed by Rong et al. (20) and discussed in Section 4.4, needs to be updated to cover a wider range of Mg (and MV) systems. Although the rules work reasonably well among close-packed structures (e.g., spinels, close-packed layered frameworks), exceptions exist, especially when considering structures that are more open (e.g., tunnel-like

frameworks such as Hollandite and postspinels) (34–36). Thus, an updated set of design rules will help accelerate the discovery of materials with facile Mg (and MV) ionic conductivity. Recently, a theoretical study has attempted to frame a new set of rules that may work well for Ca (and other large cations), but more work is required to design rules that can encompass different ionic sizes and a wide variety of host frameworks (45).

There is a significant lack of data availability for ionic mobility as compared with the data sets containing intercalation voltages, theoretical capacities, and thermodynamic stabilities that are available on open databases (147–149). While high-throughput calculations of mobility data, which are needed to create a computational mobility database, are difficult to implement, attempts can be undertaken to make available on a single platform whatever computational and experimental mobility data exists. Such a mobility database will enable the usage of statistical (and ML) techniques with fewer obstacles, which may shorten the time required for materials discovery and improve the fundamental understanding of observed diffusivity or ionic conductivity across systems. The availability of raw experimental data will especially help in minimizing the uncertainties involved in measuring transport properties, such as the variability in AC-IS measurements illustrated by Ohno et al. (128).

Apart from the classes of materials that have been studied so far as Mg conductors, a wide variety of structures and compositions remain to be explored, a few of which are mentioned here. For example, the structural versatility and the 3D diffusion characteristics of NASICON frameworks that can host Mg deserve immediate attention (150). Notably, the presence of a 3D Li ion transport pathway (rather than 1D channels) in $Li_{10}GeP_2S_{12}$ was proposed with the identification of an additional Li site through MD simulations and neutron powder diffraction. This subsequently led to the discovery of a whole class of sulfide-based Li-ion conductors, some of which have exhibited conductivities on par with liquid electrolytes (74). In this context, as illustrated in a recent article (150), Li, Mg, and Na NASICONs may exhibit substantially different phonon dispersions, which may alter the observed ionic migration, thus indicating that NASICON frameworks could act as breakthrough conductors for Mg. Similarly, borohydride materials [e.g., $Mg(BH_4)_2$] are a promising family of Mg conductors, as indicated by recent heightened scientific interest (151). However, measured conductivities should be interpreted with caution in these materials since protons and Mg may be mobile in the structure, especially at elevated temperatures. In this respect, parallel characterization of ion transport, along with a routine electrochemical measurement, should be sought to unambiguously probe Mg transport over other ions. Another class of oxides that may yet be relevant are the postspinels (34), where a recent study discovered a facile Ca-conducting postspinel (45).

DISCLOSURE STATEMENT

The authors are not aware of any affiliations, memberships, funding, or financial holdings that might be perceived as affecting the objectivity of this review.

ACKNOWLEDGMENTS

LITERATURE CITED

1. Nykvist B, Nilsson M. 2015. Rapidly falling costs of battery packs for electric vehicles. *Nat. Clim. Change* 5(4):329–32

2. Crabtree G. 2015. Perspective: the energy-storage revolution. *Nature* 526(7575):S92

3. Yaghoobnejad Asl H, Manthiram A. 2021. Toward sustainable batteries. *Nat. Sustain.* 4(5):379–80

4. Bourzac K. 2015. Batteries: 4 big questions. *Nature* 526(7575):S105

5. Jung R, Metzger M, Maglia F, Stinner C, Gasteiger HA. 2017. Oxygen release and its effect on the cycling stability of $LiNi_xMn_yCo_zO_2$ (NMC) cathode materials for Li-ion batteries. *J. Electrochem. Soc.* 164(7):A1361–77

6. Olivetti EA, Ceder G, Gaustad GG, Fu X. 2017. Lithium-ion battery supply chain considerations: analysis of potential bottlenecks in critical metals. *Joule* 1(2):229–43

7. Muldoon J, Bucur CB, Gregory T. 2014. Quest for nonaqueous multivalent secondary batteries: magnesium and beyond. *Chem. Rev.* 114(23):11683–720

8. Canepa P, Sai Gautam G, Hannah DC, Malik R, Liu M, et al. 2017. Odyssey of multivalent cathode materials: open questions and future challenges. *Chem. Rev.* 117(5):4287–341

9. Arroyo-de Dompablo ME, Ponrouch A, Johansson P, Palacín MR. 2020. Achievements, challenges, and prospects of calcium batteries. *Chem. Rev.* 120(14):6331–57

10. Davidson R, Verma A, Santos D, Hao F, Fincher C, et al. 2019. Formation of magnesium dendrites during electrodeposition. *ACS Energy Lett.* 4(2):375–76

11. Bachman JC, Muy S, Grimaud A, Chang H-H, Pour N, et al. 2016. Inorganic solid-state electrolytes for lithium batteries: mechanisms and properties governing ion conduction. *Chem. Rev.* 116(1):140–62

12. Logan ER, Dahn JR. 2020. Electrolyte design for fast-charging Li-ion batteries. *Trends Chem.* 2(4):354–66

13. Richards WD, Miara LJ, Wang Y, Kim JC, Ceder G. 2016. Interface stability in solid-state batteries. *Chem. Mater.* 28(1):266–73

14. Janek J, Zeier WG. 2016. A solid future for battery development. *Nat. Energy* 1(9):16141

15. Famprikis T, Canepa P, Dawson JA, Islam MS, Masquelier C. 2019. Fundamentals of inorganic solid-state electrolytes for batteries. *Nat. Mater.* 18(12):1278–91

16. Xiao Y, Wang Y, Bo S-H, Kim JC, Miara LJ, Ceder G. 2020. Understanding interface stability in solid-state batteries. *Nat. Rev. Mater.* 5(2):105–26

17. Muldoon J, Bucur CB, Oliver AG, Sugimoto T, Matsui M, et al. 2012. Electrolyte roadblocks to a magnesium rechargeable battery. *Energy Environ. Sci.* 5(3):5941–50

18. Canepa P, Gautam GS, Malik R, Jayaraman S, Rong Z, et al. 2015. Understanding the initial stages of reversible Mg deposition and stripping in inorganic nonaqueous electrolytes. *Chem. Mater.* 27(9):3317–25

19. Canepa P, Jayaraman S, Cheng L, Rajput NN, Richards WD, et al. 2015. Elucidating the structure of the magnesium aluminum chloride complex electrolyte for magnesium-ion batteries. *Energy Environ. Sci.* 8(12):3718–30

20. Rong Z, Malik R, Canepa P, Sai Gautam G, Liu M, et al. 2015. Materials design rules for multivalent ion mobility in intercalation structures. *Chem. Mater.* 27(17):6016–21

21. Gautam GS, Canepa P, Malik R, Liu M, Persson K, Ceder G. 2015. First-principles evaluation of multivalent cation insertion into orthorhombic V_2O_5. *Chem. Commun.* 51(71):13619–22

22. Liu M, Rong Z, Malik R, Canepa P, Jain A, et al. 2015. Spinel compounds as multivalent battery cathodes: a systematic evaluation based on *ab initio* calculations. *Energy Environ. Sci.* 8(3):964–74

23. Aurbach D, Lu Z, Schechter A, Gofer Y, Gizbar H, et al. 2000. Prototype systems for rechargeable magnesium batteries. *Nature* 407(6805):724–27

24. Gershinsky G, Yoo HD, Gofer Y, Aurbach D. 2013. Electrochemical and spectroscopic analysis of Mg^{2+} intercalation into thin film electrodes of layered oxides: V_2O_5 and MoO_3. *Langmuir* 29(34):10964–72

25. Sai Gautam G, Canepa P, Abdellahi A, Urban A, Malik R, Ceder G. 2015. The intercalation phase diagram of Mg in V_2O_5 from first-principles. *Chem. Mater.* 27(10):3733–42

26. Attias R, Salama M, Hirsch B, Pant R, Gofer Y, Aurbach D. 2019. Anion effects on cathode electro-chemical activity in rechargeable magnesium batteries: a case study of V_2O_5. *ACS Energy Lett.* 4(1):209–14

27. Yoo HD, Jokisaari JR, Yu Y-S, Kwon BJ, Hu L, et al. 2019. Intercalation of magnesium into a layered vanadium oxide with high capacity. *ACS Energy Lett.* 4(7):1528–34

28. Sun X, Bonnick P, Duffort V, Liu M, Rong Z, et al. 2016. A high capacity thiospinel cathode for Mg batteries. *Energy Environ. Sci.* 9(7):2273–77

29. Sun X, Bonnick P, Nazar LF. 2016. Layered TiS_2 positive electrode for Mg batteries. *ACS Energy Lett.* 1(1):297–301

30. Bonnick P, Sun X, Lau K-C, Liao C, Nazar LF. 2017. Monovalent versus divalent cation diffusion in thiospinel Ti_2S_4. *J. Phys. Chem. Lett.* 8(10):2253–57

31. Emly A, Van der Ven A. 2015. Mg intercalation in layered and spinel host crystal structures for Mg batteries. *Inorg. Chem.* 54(9):4394–402

32. Kolli SK, Van der Ven A. 2018. First-principles study of spinel $MgTiS_2$ as a cathode material. *Chem. Mater.* 30(7):2436–42

33. Chen T, Sai Gautam G, Huang W, Ceder G. 2018. First-principles study of the voltage profile and mobility of Mg intercalation in a chromium oxide spinel. *Chem. Mater.* 30(1):153–62

34. Hannah DC, Sai Gautam G, Canepa P, Rong Z, Ceder G. 2017. Magnesium ion mobility in post-spinels accessible at ambient pressure. *Chem. Commun.* 53(37):5171–74

35. Arthur TS, Zhang R, Ling C, Glans P-A, Fan X, et al. 2014. Understanding the electrochemical mech-anism of K-αMnO_2 for magnesium battery cathodes. *ACS Appl. Mater. Interfaces* 6(10):7004–8

36. Zhang R, Yu X, Nam K-W, Ling C, Arthur TS, et al. 2012. α-MnO_2 as a cathode material for recharge-able Mg batteries. *Electrochem. Commun.* 23:110–13

37. Kim C, Phillips PJ, Key B, Yi T, Nordlund D, et al. 2015. Direct observation of reversible magnesium ion intercalation into a spinel oxide host. *Adv. Mater.* 27(22):3377–84

38. Sai Gautam G, Canepa P, Urban A, Bo S-H, Ceder G. 2017. Influence of inversion on Mg mobility and electrochemistry in spinels. *Chem. Mater.* 29(18):7918–30

39. Bayliss RD, Key B, Sai Gautam G, Canepa P, Kwon BJ, et al. 2020. Probing Mg migration in spinel oxides. *Chem. Mater.* 32(2):663–70

40. Forero-Saboya J, Davoisne C, Dedryvère R, Yousef I, Canepa P, Ponrouch A. 2020. Understanding the nature of the passivation layer enabling reversible calcium plating. *Energy Environ. Sci.* 13(10):3423–31

41. Sai Gautam G, Canepa P, Richards WD, Malik R, Ceder G. 2016. Role of structural H_2O in intercalation electrodes: the case of Mg in nanocrystalline xerogel-V_2O_5. *Nano Lett.* 16(4):2426–31

42. Kundu D, Adams BD, Duffort V, Vajargah SH, Nazar LF. 2016. A high-capacity and long-life aqueous rechargeable zinc battery using a metal oxide intercalation cathode. *Nat. Energy* 1(10):16119

43. Chen T, Sai Gautam G, Canepa P. 2019. Ionic transport in potential coating materials for Mg batteries. *Chem. Mater.* 31(19):8087–99

44. Chen T, Ceder G, Sai Gautam G, Canepa P. 2019. Evaluation of Mg compounds as coating materials in Mg batteries. *Front. Chem.* 7:24

45. Lu W, Wang J, Sai Gautam G, Canepa P. 2021. Searching ternary oxides and chalcogenides as positive electrodes for calcium batteries. *Chem. Mater.* 33(14):5809–21

46. Canepa P, Bo S-H, Sai Gautam G, Key B, Richards WD, et al. 2017. High magnesium mobility in ternary spinel chalcogenides. *Nat. Commun.* 8(1):1759

47. Canepa P, Sai Gautam G, Broberg D, Bo S-H, Ceder G. 2017. Role of point defects in spinel Mg chalcogenide conductors. *Chem. Mater.* 29(22):9657–67

48. Wang L-P, Zhao-Karger Z, Klein F, Chable J, Braun T, et al. 2019. $MgSc_2Se_4$—a magnesium solid ionic conductor for all-solid-state Mg batteries? *ChemSusChem* 12(10):2286–93

49. Gorai P, Famprikis T, Gill BS, Stevanovic V, Canepa P. 2021. The devil is in the defects: electronic conductivity in solid electrolytes. *Chem. Mater.* 33(18):7484–98

50. Fick DA. 1855. V. On liquid diffusion. *Lond. Edinb. Dublin Philos. Mag. J. Sci.* 10(63):30–39

51. Fick A. 1855. Ueber Diffusion. *Ann. Phys.* 170(1):59–86

52. Balluffi RW, Allen SM, Carter WC. 2005. Atomic models for diffusion. In *Kinetics of Materials*, pp. 145–61. Hoboken, NJ: John Wiley & Sons

53. Van der Ven A, Ceder G, Asta M, Tepesch PD. 2001. First-principles theory of ionic diffusion with nondilute carriers. *Phys. Rev. B* 64(18):184307

54. Holstein T. 1959. Studies of polaron motion. *Ann. Phys.* 8(3):343–89

55. Reticcioli M, Diebold U, Kresse G, Franchini C. 2019. Small polarons in transition metal oxides. In *Handbook of Materials Modeling*, ed. W Andreoni, S Yip, pp. 1–39. Cham, Switz.: Springer Int. Publ.

56. Maxisch T, Zhou F, Ceder G. 2006. *Ab initio* study of the migration of small polarons in olivine Li_xFePO_4 and their association with lithium ions and vacancies. *Phys. Rev. B* 73(10):104301

57. Van der Ven A, Aydinol MK, Ceder G, Kresse G, Hafner J. 1998. First-principles investigation of phase stability in Li_xCoO_2. *Phys. Rev. B* 58(6):2975–87

58. Amores M, Ashton TE, Baker PJ, Cussen EJ, Corr SA. 2016. Fast microwave-assisted synthesis of Li-stuffed garnets and insights into Li diffusion from muon spin spectroscopy. *J. Mater. Chem. A* 4(5):1729–36

59. Månsson M, Sugiyama J. 2013. Muon-spin relaxation study on Li- and Na-diffusion in solids. *Phys. Scr.* 88(6):068509

60. McClelland I, Booth SG, El-Shinawi H, Johnston BIJ, Clough J, et al. 2021. In situ diffusion measurements of a NASICON-structured all-solid-state battery using muon spin relaxation. *ACS Appl. Energy Mater.* 4(2):1527–36

61. Powell AS, Lord JS, Gregory DH, Titman JJ. 2009. Muon spin relaxation studies of lithium nitridometallate battery materials: muon trapping and lithium ion diffusion. *J. Phys. Chem. C* 113(48):20758–63

62. Bée M. 2003. Localized and long-range diffusion in condensed matter: state of the art of QENS studies and future prospects. *Chem. Phys.* 292(2–3):121–41

63. Nozaki H, Harada M, Ohta S, Watanabe I, Miyake Y, et al. 2014. Li diffusive behavior of garnet-type oxides studied by muon-spin relaxation and QENS. *Solid State Ion.* 262:585–88

64. Kulkarni NS, Bruce Warmack RJ, Radhakrishnan B, Hunter JL, Sohn Y, et al. 2014. Overview of SIMS-based experimental studies of tracer diffusion in solids and application to Mg self-diffusion. *J. Phase Equilib. Diffus.* 35(6):762–78

65. Kuwata N, Hasegawa G, Maeda D, Ishigaki N, Miyazaki T, Kawamura J. 2020. Tracer diffusion coefficients of Li ions in $Li_xMn_2O_4$ thin films observed by isotope exchange secondary ion mass spectrometry. *J. Phys. Chem. C* 124(42):22981–92

66. Masuda H, Ishida N, Ogata Y, Ito D, Fujita D. 2018. In situ visualization of Li concentration in all-solid-state lithium ion batteries using time-of-flight secondary ion mass spectrometry. *J. Power Sourc.* 400:527–32

67. Macdonald JR, Johnson WB. 2005. Fundamentals of impedance spectroscopy. In *Impedance Spectroscopy*, ed. E Barsoukov, JR Macdonald, pp. 1–26. Hoboken, NJ: John Wiley & Sons

68. Halim ZA, Adnan SBRS, Mohamed NS. 2016. Effect of sintering temperature on the structural, electrical and electrochemical properties of novel $Mg_{0.5}Si_2(PO_4)_3$ ceramic electrolytes. *Ceram. Int.* 42(3):4452–61

69. Masquelier C, Croguennec L. 2013. Polyanionic (phosphates, silicates, sulfates) frameworks as electrode materials for rechargeable Li (or Na) batteries. *Chem. Rev.* 113(8):6552–91

70. Anuar NK, Adnan SBRS, Mohamed NS. 2014. Characterization of $Mg_{0.5}Zr_2(PO_4)_3$ for potential use as electrolyte in solid state magnesium batteries. *Ceram. Int.* 40(8):13719–27

71. Fleig J. 2003. Microelectrodes in solid state ionics. *Solid State Ion.* 161(3–4):279–89

72. Rettenwander D, Welzl A, Pristat S, Tietz F, Taibl S, et al. 2016. A microcontact impedance study on NASICON-type $Li_{1+x}Al_xTi_{2-x}(PO_4)_3$ ($0 \le x \le 0.5$) single crystals. *J. Mater. Chem. A* 4(4):1506–13

73. Jamnik J, Maier J. 2001. Generalised equivalent circuits for mass and charge transport: chemical capacitance and its implications. *Phys. Chem. Chem. Phys.* 3(9):1668–78

74. Bachman JC, Muy S, Grimaud A, Chang H, Pour N, et al. 2016. Inorganic solid-state electrolytes for lithium batteries: mechanisms and properties governing ion conduction. *Chem. Rev.* 116(1):140–62

75. Gao Y, Nolan AM, Du P, Wu Y, Yang C, et al. 2020. Classical and emerging characterization techniques for investigation of ion transport mechanisms in crystalline fast ionic conductors. *Chem. Rev.* 120(13):5954–6008

76. Anuar NK, Adnan SBRS, Jaafar MH, Mohamed NS. 2016. Studies on structural and electrical properties of $Mg_{0.5+y}$ $(Zr_{2-y}Fe_y)_2(PO_4)_3$ ceramic electrolytes. *Ionics* 22(7):1125–33

77. Anuar NK, Mohamed NS. 2016. Structural and electrical properties of novel $Mg_{0.9+0.5y}$ $Zn_{0.4}Al_yZr_{1.6-y}$ $(PO_4)_3$ ceramic electrolytes synthesized via nitrate sol-gel method. *J. Sol-Gel Sci. Technol.* 80(2):249–58

78. Deng Z, Sai Gautam G, Kolli SK, Chotard J-N, Cheetham AK, et al. 2020. Phase behavior in rhombohedral NaSiCON electrolytes and electrodes. *Chem. Mater.* 32(18):7908–20

79. Kamaya N, Homma K, Yamakawa Y, Hirayama M, Kanno R, et al. 2011. A lithium superionic conductor. *Nat. Mater.* 10(9):682–86

80. Hamao N, Kataoka K, Kijima N, Akimoto J. 2016. Synthesis, crystal structure and conductive properties of garnet-type lithium ion conductor Al-free $Li_{7-x}La_3Zr_{2-x}Ta_xO_{12}$ ($0 \leq x \leq 0.6$). *J. Ceram. Soc. Jpn.* 124(6):678–83

81. Bloembergen N, Purcell EM, Pound RV. 1948. Relaxation effects in nuclear magnetic resonance absorption. *Phys. Rev.* 73(7):679–712

82. Posch P, Lunghammer S, Berendts S, Ganschow S, Redhammer GJ, et al. 2020. Ion dynamics in Al-stabilized $Li_7La_3Zr_2O_{12}$ single crystals – macroscopic transport and the elementary steps of ion hopping. *Energy Storage Mater.* 24:220–28

83. Bottke P, Rettenwander D, Schmidt W, Amthauer G, Wilkening M. 2015. Ion dynamics in solid electrolytes: NMR reveals the elementary steps of Li^+ hopping in the garnet $Li_{6.5}La_3Zr_{1.75}Mo_{0.25}O_{12}$. *Chem. Mater.* 27(19):6571–82

84. Epp V, Gün Ö, Deiseroth H-J, Wilkening M. 2013. Highly mobile ions: low-temperature NMR directly probes extremely fast Li^+ hopping in argyrodite-type Li_6PS_5Br. *J. Phys. Chem. Lett.* 4(13):2118–23

85. Burankova T, Roedern E, Maniadaki AE, Hagemann H, Rentsch D, et al. 2018. Dynamics of the coordination complexes in a solid-state Mg electrolyte. *J. Phys. Chem. Lett.* 9(22):6450–55

86. Heere M, Hansen A-L, Payandeh S, Aslan N, Gizer G, et al. 2020. Dynamics of porous and amorphous magnesium borohydride to understand solid state Mg-ion-conductors. *Sci. Rep.* 10(1):9080

87. Sears VF. 1992. Neutron scattering lengths and cross sections. *Neutron News* 3(3):26–37

88. Skripov AV, Soloninin AV, Ley MB, Jensen TR, Filinchuk Y. 2013. Nuclear magnetic resonance studies of BH_4 reorientations and Li diffusion in $LiLa(BH_4)_3Cl$. *J. Phys. Chem. C* 117(29):14965–72

89. Weppner W, Huggins RA. 1977. Determination of the kinetic parameters of mixed-conducting electrodes and application to the system Li_3Sb. *J. Electrochem. Soc.* 124(10):1569–78

90. Bonnick P, Blanc L, Vajargah SH, Lee C-W, Sun X, et al. 2018. Insights into Mg^{2+} intercalation in a zero-strain material: thiospinel $Mg_xZr_2S_4$. *Chem. Mater.* 30(14):4683–93

91. Arbi K, Hoelzel M, Kuhn A, García-Alvarado F, Sanz J. 2013. Structural factors that enhance lithium mobility in fast-ion $Li_{1+x}Ti_{2-x}Al_x(PO_4)_3$ ($0 \leq x \leq 0.4$) conductors investigated by neutron diffraction in the temperature range 100–500 K. *Inorg. Chem.* 52(16):9290–96

92. Pérez-Estébanez M, Isasi-Marín J, Többens DM, Rivera-Calzada A, León C. 2014. A systematic study of Nasicon-type $Li_{1+x}M_xTi_{2-x}(PO_4)_3$ (M: Cr, Al, Fe) by neutron diffraction and impedance spectroscopy. *Solid State Ion.* 266:1–8

93. Bo S-H, Grey CP, Khalifah PG. 2015. Defect-tolerant diffusion channels for Mg^{2+} ions in ribbon-type borates: structural insights into potential battery cathodes $MgVBO_4$ and $Mg_xFe_{2-x}B_2O_5$. *Chem. Mater.* 27(13):4630–39

94. Yin L, Kwon BJ, Choi Y, Bartel CJ, Yang M, et al. 2021. Operando X-ray diffraction studies of the Mg-ion migration mechanisms in spinel cathodes for rechargeable Mg-ion batteries. *J. Am. Chem. Soc.* 143(28):10649–58

95. Jónsson H, Mills G, Jacobsen KW. 1998. Nudged elastic band method for finding minimum energy paths of transitions. In *Classical and Quantum Dynamics in Condensed Phase Simulations*, ed. BJ Berne, G Ciccotti, DF Coker, pp. 385–404. Singapore: World Sci.

96. Henkelman G, Uberuaga BP, Jónsson H. 2000. A climbing image nudged elastic band method for finding saddle points and minimum energy paths. *J. Chem. Phys.* 113(22):9901–4

97. Van der Ven A, Ceder G, Asta M, Tepesch PD. 2001. First-principles theory of ionic diffusion with nondilute carriers. *Phys. Rev. B* 64(18):184307

98. Van der Ven A, Bhattacharya J, Belak AA. 2013. Understanding Li diffusion in Li-intercalation compounds. *Acc. Chem. Res.* 46(5):1216–25

99. He X, Zhu Y, Epstein A, Mo Y. 2018. Statistical variances of diffusional properties from ab initio molecular dynamics simulations. *NPJ Comput. Mater.* 4(1):18

100. Frenkel D, Smit B. 2002. *Understanding Molecular Simulation*. San Diego, CA: Acad. Press

101. Car R, Parrinello M. 1985. Unified approach for molecular dynamics and density-functional theory. *Phys. Rev. Lett.* 55(22):2471–74

102. Mo Y, Ong SP, Ceder G. 2012. First principles study of the $Li_{10}GeP_2S_{12}$ lithium super ionic conductor material. *Chem. Mater.* 24(1):15–17

103. He X, Zhu Y, Mo Y. 2017. Origin of fast ion diffusion in super-ionic conductors. *Nat. Commun.* 8(1):15893

104. Materzanini G, Kahle L, Marcolongo A, Marzari N. 2021. High Li-ion conductivity in tetragonal LGPO: a comparative first-principles study against known LISICON and LGPS phases. *Phys. Rev. Mater.* 5(3):035408

105. Lewis GV, Catlow CRA. 1985. Potential models for ionic oxides. *J. Phys. C* 18(6):1149–61

106. Ercolessi F, Adams JB. 1994. Interatomic potentials from first-principles calculations: the force-matching method. *Europhys. Lett.* 26(8):583–88

107. Wang C, Aoyagi K, Wisesa P, Mueller T. 2020. Lithium ion conduction in cathode coating materials from on-the-fly machine learning. *Chem. Mater.* 32(9):3741–52

108. Artrith N, Urban A. 2016. An implementation of artificial neural-network potentials for atomistic materials simulations: performance for TiO_2. *Comput. Mater. Sci.* 114:135–50

109. Artrith N, Behler J. 2012. High-dimensional neural network potentials for metal surfaces: a prototype study for copper. *Phys. Rev. B* 85(4):045439

110. Artrith N, Urban A, Ceder G. 2017. Efficient and accurate machine-learning interpolation of atomic energies in compositions with many species. *Phys. Rev. B* 96(1):014112

111. Shapeev AV. 2016. Moment tensor potentials: a class of systematically improvable interatomic potentials. *Multiscale Model. Simul.* 14(3):1153–73

112. Zuo Y, Chen C, Li X, Deng Z, Chen Y, et al. 2020. Performance and cost assessment of machine learning interatomic potentials. *J. Phys. Chem. A* 124(4):731–45

113. Bartók AP, Payne MC, Kondor R, Csányi G. 2010. Gaussian approximation potentials: the accuracy of quantum mechanics, without the electrons. *Phys. Rev. Lett.* 104(13):136403

114. Thompson AP, Swiler LP, Trott CR, Foiles SM, Tucker GJ. 2015. Spectral neighbor analysis method for automated generation of quantum-accurate interatomic potentials. *J. Comput. Phys.* 285:316–30

115. Behler J, Parrinello M. 2007. Generalized neural-network representation of high-dimensional potential-energy surfaces. *Phys. Rev. Lett.* 98(14):146401

116. Rong Z, Kitchaev D, Canepa P, Huang W, Ceder G. 2016. An efficient algorithm for finding the minimum energy path for cation migration in ionic materials. *J. Chem. Phys.* 145(7):074112

117. Bölle FT, Mathiesen NR, Nielsen AJ, Vegge T, Garcia-Lastra JM, Castelli IE. 2020. Autonomous discovery of materials for intercalation electrodes. *Batter. Supercaps* 3(6):488–98

118. Chang JH, Jørgensen PB, Loftager S, Bhowmik A, Lastra JMG, Vegge T. 2021. On-the-fly assessment of diffusion barriers of disordered transition metal oxyfluorides using local descriptors. *Electrochim. Acta* 388:138551

119. Bortz AB, Kalos MH, Lebowitz JL. 1975. A new algorithm for Monte Carlo simulation of Ising spin systems. *J. Comput. Phys.* 17(1):10–18

120. Van der Ven A, Thomas JC, Puchala B, Natarajan AR. 2018. First-principles statistical mechanics of multicomponent crystals. *Annu. Rev. Mater. Res.* 48:27–55

121. Sanchez JM, Ducastelle F, Gratias D. 1984. Generalized cluster description of multicomponent systems. *Phys. A Stat. Mech. Appl.* 128(1–2):334–50

122. Rong Z, Malik R, Canepa P, Sai Gautam G, Liu M, et al. 2015. Materials design rules for multivalent ion mobility in intercalation structures. *Chem. Mater.* 27(17):6016–21

123. Canepa P, Bo S-H, Sai Gautam G, Key B, Richards WD, et al. 2017. High magnesium mobility in ternary spinel chalcogenides. *Nat. Commun.* 8(1):1759

124. Koettgen J, Bartel CJ, Ceder G. 2020. Computational investigation of chalcogenide spinel conductors for all-solid-state Mg batteries. *Chem. Commun.* 56(13):1952–55

125. Dillenz M, Sotoudeh M, Euchner H, Groß A. 2020. Screening of charge carrier migration in the $MgSc_2Se_4$ spinel structure. *Front. Energy Res.* 8:584654

126. Han F, Westover AS, Yue J, Fan X, Wang F, et al. 2019. High electronic conductivity as the origin of lithium dendrite formation within solid electrolytes. *Nat. Energy* 4(3):187–96

127. Huggins RA. 2002. Simple method to determine electronic and ionic components of the conductivity in mixed conductors a review. *Ionics* 8(3–4):300–13

128. Ohno S, Bernges T, Buchheim J, Duchardt M, Hatz A-K, et al. 2020. How certain are the reported ionic conductivities of thiophosphate-based solid electrolytes? An interlaboratory study. *ACS Energy Lett.* 5(3):910–15

129. Gao Y, Li N, Wu Y, Yang W, Bo S. 2021. Rethinking the design of ionic conductors using Meyer–Neldel–conductivity plot. *Adv. Energy Mater.* 11(13):2100325

130. Metselaar R, Oversluizen G. 1984. The Meyer-Neldel rule in semiconductors. *J. Solid State Chem.* 55(3):320–26

131. Wilkening M, Heitjans P. 2012. From micro to macro: access to long-range Li^+ diffusion parameters in solids via microscopic $^{6,7}Li$ spin-alignment echo NMR spectroscopy. *ChemPhysChem* 13(1):53–65

132. Holmes L, Peng L, Heinmaa I, O'Dell LA, Smith ME, et al. 2008. Variable-temperature ^{17}O NMR study of oxygen motion in the anionic conductor $Bi_{26}Mo_{10}O_{69}$. *Chem. Mater.* 20(11):3638–48

133. Halat DM, Dunstan MT, Gaultois MW, Britto S, Grey CP. 2018. Study of defect chemistry in the system $La_{2-x}Sr_xNiO_{4+\delta}$ by ^{17}O solid-state NMR spectroscopy and Ni K-edge XANES. *Chem. Mater.* 30(14):4556–70

134. Kim G, Griffin JM, Blanc F, Haile SM, Grey CP. 2015. Characterization of the dynamics in the protonic conductor CsH_2PO_4 by ^{17}O solid-state NMR spectroscopy and first-principles calculations: correlating phosphate and protonic motion. *J. Am. Chem. Soc.* 137(11):3867–76

135. Kim G, Blanc F, Hu Y-Y, Grey CP. 2013. Understanding the conduction mechanism of the protonic conductor CsH_2PO_4 by solid-state NMR spectroscopy. *J. Phys. Chem. C* 117(13):6504–15

136. Stone NJ. 2016. Table of nuclear electric quadrupole moments. *At. Data Nucl. Data Tables* 111–112:1–28

137. Dupree R, Smith ME. 1988. Solid-state magnesium-25 n.m.r. spectroscopy. *J. Chem. Soc. Chem. Commun.* 22:1483–85

138. Freitas JCC, Smith ME. 2012. Recent advances in solid-state ^{25}Mg NMR spectroscopy. In *Annual Reports on NMR Spectroscopy*, Vol. 75, pp. 25–114. Oxford, UK: Acad. Press

139. Barnes TA, Wan LF, Kent PRC, Prendergast D. 2018. Hybrid DFT investigation of the energetics of Mg ion diffusion in α-MoO_3. *Phys. Chem. Chem. Phys.* 20(38):24877–84

140. McColl K, Corà F. 2019. Mg^{2+} storage and mobility in anatase TiO_2: the role of frustrated coordination. *J. Mater. Chem. A* 7(8):3704–13

141. McColl K, Corà F. 2019. Phase stability of intercalated V_2O_5 battery cathodes elucidated through the Goldschmidt tolerance factor. *Phys. Chem. Chem. Phys.* 21(15):7732–44

142. Dawson JA, Canepa P, Famprikis T, Masquelier C, Islam MS. 2018. Atomic-scale influence of grain boundaries on Li-ion conduction in solid electrolytes for all-solid-state batteries. *J. Am. Chem. Soc.* 140(1):362–68

143. Dawson JA, Canepa P, Clarke MJ, Famprikis T, Ghosh D, Islam MS. 2019. Toward understanding the different influences of grain boundaries on ion transport in sulfide and oxide solid electrolytes. *Chem. Mater.* 31(14):5296–304

144. Butler KT, Sai Gautam G, Canepa P. 2019. Designing interfaces in energy materials applications with first-principles calculations. *NPJ Comput. Mater.* 5(1):19

145. Mueller T, Hernandez A, Wang C. 2020. Machine learning for interatomic potential models. *J. Chem. Phys.* 152(5):050902

146. Caro MA. 2019. Optimizing many-body atomic descriptors for enhanced computational performance of machine learning based interatomic potentials. *Phys. Rev. B* 100(2):024112

147. Jain A, Ong SP, Hautier G, Chen W, Richards WD, et al. 2013. The materials project: a materials genome approach to accelerating materials innovation. *APL Mater*. 1(1):011002

148. Saal JE, Kirklin S, Aykol M, Meredig B, Wolverton C. 2013. Materials design and discovery with high-throughput density functional theory: the open quantum materials database (OQMD). *JOM* 65(11):1501–9

149. Kirklin S, Saal JE, Meredig B, Thompson A, Doak JW, et al. 2015. The open quantum materials database (OQMD): assessing the accuracy of DFT formation energies. *NPJ Comput. Mater.* 1(1):15010

150. Jaschin PW, Gao Y, Li Y, Bo S-H. 2020. A materials perspective on magnesium-ion-based solid-state electrolytes. *J. Mater. Chem. A* 8(6):2875–97

151. Mohtadi R, Matsui M, Arthur TS, Hwang S-J. 2012. Magnesium borohydride: from hydrogen storage to magnesium battery. *Angew. Chem. Int. Ed.* 51(39):9780–83

Contents

Indexes

Errata

An online log of corrections to *Annual Review of Materials Research* articles may be
found at http://www.annualreviews.org/errata/matsci